JGR Planets

RESEARCH ARTICLE
10.1029/2019JE005937

Key Points:
- We applied the Markov chain Monte Carlo (MCMC) method for the first time to invert for regional loading and flexural parameters on Mars
- The choice of a reasonable loading style assumption is critical for obtaining meaningful effective elastic lithospheric thickness estimates
- The *Te* and surface density estimates are consistent with a model of global lithospheric thickening and the expected loading materials

Supporting Information:
- Supporting Information S1

Correspondence to:
J. Lin,
jlin@whoi.edu

Citation:
Ding, M., Lin, J., Gu, C., Huang, Q., & Zuber, M. T. (2019). Variations in Martian lithospheric strength based on gravity/topography analysis. *Journal of Geophysical Research: Planets*, *124*. https://doi.org/10.1029/2019JE005937

Received 16 MAR 2019
Accepted 7 NOV 2019
Accepted article online 20 NOV 2019

Variations in Martian Lithospheric Strength Based on Gravity/Topography Analysis

Min Ding[1,2,3], Jian Lin[4,5], Chen Gu[6], Qinghua Huang[2], and Maria T. Zuber[6]

[1]State Key Laboratory of Lunar and Planetary Sciences, Macau University of Science and Technology, Macau, China, [2]School of Earth and Space Sciences, Peking University, Beijing, China, [3]MIT/WHOI Joint Program, Woods Hole Oceanographic Institution, Woods Hole, MA, USA, [4]Department of Geology and Geophysics, Woods Hole Oceanographic Institution, Woods Hole, MA, USA, [5]Key Laboratory of Ocean and Marginal Sea Geology, South China Sea Institute of Oceanology, Chinese Academy of Sciences, Guangzhou, China, [6]Department of Earth, Atmospheric and Planetary Sciences, Massachusetts Institute of Technology, Cambridge, MA, USA

Abstract We applied localized gravity/topography admittance and correlation analysis, as well as the Markov chain Monte Carlo method, to invert for loading and flexural parameters of 21 subregions on Mars with five distinct tectonic types. The loading styles of the five tectonic types are distinct: The surface and subsurface loading in the polar and plain regions can be assumed to be largely uncorrelated, in contrast to the correlated loading associated with the volcanic montes and Valles Marineris. For the impact basins, we consider the initial topographic depression and mantle plug before postimpact surface loading. Our analyses yield four main results: (1) The inverted effective lithospheric thickness (*Te*) is highly dependent on assumptions of loading type. (2) There is a trend of increasing *Te* from the Noachian southern highlands (20–60 km) to the Hesperian northern lowlands (>90 km) and from the Hesperian Elysium Mons (<55 km) to the Hesperian/Amazonian Olympus Mons (>105 km). These *Te* estimates are consistent with the thermal states at the time of loading, corresponding to a global secular cooling history with decreasing heat flux. (3) Our analyses suggest high-density basaltic surface loading at the volcanic montes and Isidis basin, in contrast to the low-density sedimentary surface loading at the Utopia and Argyre basins. (4) We find some degree of correlation between the surface and subsurface loading for the northern polar cap and the northern plains, likely due to earlier, larger polar deposits and ancient buried features, respectively.

Plain Language Summary Before the availability of seismic and heat flow data acquired by NASA's InSight mission, gravity and topography data have been the main geophysical measurements with which to unravel the Martian interior structure, geologic history, and thermal evolution. The improved resolution of the recent gravity models helps to reveal the spatial variability in crustal structure and lithospheric strength. As the gravity interpretation is inherently nonunique, a priori knowledge and reasonable assumptions on the tectonic loading scenario are required to invert for the lithospheric strength. The commonly used thin-plate flexural model assumes that the lithosphere behaves as an elastic shell when subjected to surface and subsurface loading. In this study, we developed thin-plate flexural models for polar and plain regions, for volcanic montes and valley regions, and for impact basins with different loading scenarios. We also applied a state-of-the-art Bayesian inversion method to improve the uncertainty estimation of the model parameters. Comparison with previous studies shows that the estimation of the key parameters, including the effective elastic lithospheric thickness (*Te*), is highly dependent on the assumed loading scenario and less significantly on the chosen uncertainty estimation method. However, the relative magnitude of the model parameters among regions is reliable.

1. Introduction

The strength of the lithosphere is one of the key parameters that can be used to constrain the thermal evolution of a planet and its tectonic, magmatic, and geological processes (e.g., Grott & Breuer, 2008, 2009, 2010; Kiefer & Li, 2009; Plesa et al., 2015, 2016; Solomon & Head, 1990). The effective elastic thickness (*Te*) of the Martian lithosphere has been determined by comparing flexural models with observed fault characteristics (e.g., Comer et al., 1985; Schultz & Lin, 2001) or substrata deflection as constrained by radar sounding data (Phillips et al., 2008; Plaut et al., 2007). Since 1979, when Martian gravity models became available from the Viking and Mariner 9 spacecraft Doppler tracking data (Christensen & Balmino, 1981), *Te* has also been determined by the relationship between gravity and topography (Anderson & Grimm, 1998; Banerdt et al., 1982; Janle & Erkul, 1991; Sleep & Phillips, 1985; Turcotte et al., 1981). The reliability of the regional *Te* estimates has been greatly improved by using gravity models with lower noise and increased spatial resolution.

Subsequent studies have used the gravity models from the Mars Global Surveyor and Mars Reconnaissance Orbiter missions to investigate regional *Te* variations in great detail. In comparison with spatial studies (Arkani-Hamed, 2000; Johnson et al., 2000), the inverse spectral method, as reviewed by Wieczorek (2007), Simons and Olhede (2013), Audet (2014), and Kirby (2014), has been more commonly applied. In this method, the regional *Te* estimate notably depends on the loading type assumption (i.e., the phase difference between the surface and subsurface loading, α). The assumption of perfectly correlated loading (i.e., $\alpha = \pm 1$) can be justified when the observed correlation spectra values are close to 1. This situation has been found in the volcanic montes and Valles Marineris of Mars (Belleguic et al., 2005; Beuthe et al., 2012; Grott & Wieczorek, 2012; McGovern et al., 2002). In contrast, the observed correlation spectra for polar and plain regions deviate markedly from 1 (Johnson et al., 2000; McGovern et al., 2002); therefore, the surface and subsurface loading must have phase differences. In this case, an end-member model is that the surface and subsurface loading is independent in phase (i.e., $\alpha = 0$), as suggested by Forsyth (1985). Thus, the loading style assumption is critical for reliable flexural parameter estimation.

Recent studies have also highlighted the necessity to jointly invert the admittance and correlation spectra and to apply localization windows consistently to the data and models (e.g., Crosby, 2007; Kirby, 2014; Wieczorek, 2007). Furthermore, McGovern et al. (2002) found that the finite-amplitude correction in gravity calculation is required to reproduce the gravity admittance observations for volcanic montes with large topographic slopes. All the above observational and technical considerations suggest that different localized flexural models are necessary for varied tectonic types.

In this study, we conducted localized gravity/topography admittance and correlation analysis to invert for loading and flexural parameters of 21 subregions on Mars, using the latest Martian gravity model JGMRO120d. This study is unique in that we adopted suitable loading type assumptions and localization methods for individual subregions with five distinctive tectonic settings. This study is also the first to apply Bayesian inference with the Markov chain Monte Carlo (MCMC) algorithm to improve the uncertainty estimation of Martian loading and flexural parameters.

2. Data and Method

2.1. Data and Localized Spectral Analysis

We used the latest gravity model JGMRO120d of spherical and harmonic degree and order 120 (Figure 1b) (Konopliv et al., 2016), with an addition of 10 more degrees from the previous gravity models used by Beuthe et al. (2012) and Audet (2014) and 35 more degrees from the models used by McGovern et al. (2002, 2004) and Belleguic et al. (2005). This latest gravity model is interpretable to a maximum degree of 90 (corresponding to a spatial block size resolution of ~118 km), beyond which a significant observational error exists in the gravity model (Figure S1). We used the topography model MarsTopo719 (Figure 1a) from the Mars Orbiter Laser Altimeter measurements (Smith et al., 2001; Zuber et al., 1992) and truncated it to degree 90 to be consistent with that of the gravity data.

Two spectral functions have been used to quantify the relationships between gravity and topography fields (Audet, 2014; Kirby, 2014; Simons & Olhede, 2013; Wieczorek, 2007): The admittance $Z(l)$ measures the isostactic response of gravity to topography, while the correlation $\gamma(l)$ measures the phase relationship between gravity and topography:

$$Z(l) = \frac{S_{gh}(l)}{S_{hh}(l)}, \tag{1}$$

$$\gamma(l) = S_{gh}(l) / \sqrt{S_{gg}(l) S_{hh}(l)}, \tag{2}$$

where $S_{gh}(l) = \sum_{m=-l}^{l} g_{lm} h_{lm}$, $S_{gg}(l) = \sum_{m=-l}^{l} g_{lm}^2$, and $S_{hh}(l) = \sum_{m=-l}^{l} h_{lm}^2$ are the cross-power and power spectra of the observed gravity and topography fields with spherical harmonic coefficients g_{lm} and h_{lm} for a degree l and

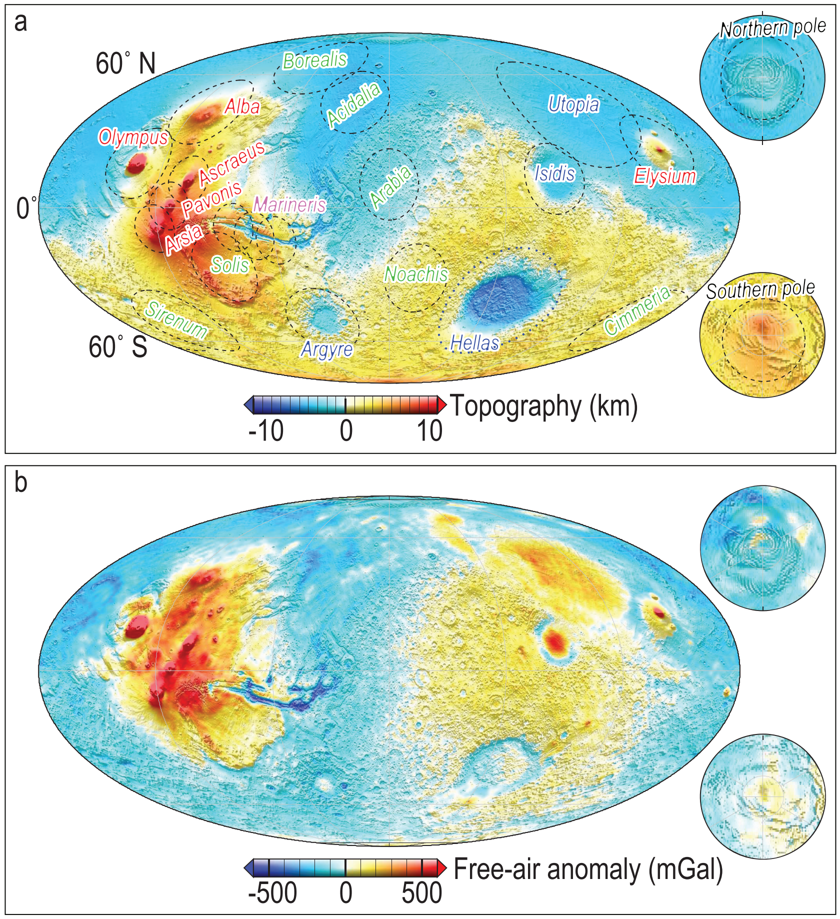

Figure 1. Global map views of Mars' (a) topography from MarsTopo719, referenced to the geoid. Dashed circles indicate the boundaries of the localized windows for the 21 investigated subregions with five distinct tectonic types. Green, red, blue, magenta, and gray text colors correspond to regions of different tectonic types, that is, plains, volcanic, impact basins, rift valleys, and polar caps, respectively. The Hellas basin is marked by a blue dotted circle because it is not modeled in this study but used as the reference initial topography for the Utopia basin (section 2.3 and supporting information Text S3). (b) Radial free-air gravity anomaly from JGMRO120d.

order m. The corresponding standard errors of the admittance and correlation have been quantified by Bendat and Piersol (2010):

$$\sigma_Z(l) = \left|\frac{Z(l)}{\gamma(l)}\right| \sqrt{\frac{1-\gamma(l)^2}{2l}}\,, \tag{3}$$

$$\sigma_\gamma(l) = \frac{1-\gamma(l)^2}{\sqrt{2l}}. \tag{4}$$

The derivation of equation (4) requires application of the uncertainty propagation rule from the equation for coherence (the square of the correlation).

To localize the gravity and topography data for the target subregions (circles with dashed curves in Figure 1a), we applied the spatiospectral localization technique of Wieczorek and Simons (2005) using SHTOOLS2.8 software. The localization window retains the original gravity and topography signature in the center of a given cap region but gradually filters out data outside the region (Figure S2) with a concentration factor (λ) of more than 99%. The angular diameter $2\theta_0$ and spectral bandwidth L_{win} of the localization cap windows used in analyzing the varied subregions are listed in Table 2. We used multiple windows (Table 2) for plains to cover their broader and noncircular spatial extent.

The localized spectrum is a smoothed version of the global spectrum $S_{gh}(l)$. When the two global fields, g_{lm} and h_{lm}, are generated by an uncorrelated stochastic process, the relationship between the localized spectrum $\langle S_{\Gamma H}(l)\rangle$ and the global spectrum $S_{gh}(l)$ follows (Wieczorek & Simons, 2005, 2007):

$$\langle S_{\Gamma H}(l)\rangle = \sum_{j=0}^{L_{\mathrm{win}}} S_{ww}(j) \sum_{i=|l-j|}^{l+j} S_{gh}(i)\left(C_{j0i0}^{l0}\right)^2, \tag{5}$$

where $\langle\cdots\rangle$ denotes the expectation operator, $S_{ww}(l)$ is the power spectra of the localization window, and C_{j0i0}^{l0} is a Clebsch-Gordan coefficient. This equation shows that $\langle S_{\Gamma H}(l)\rangle$ at degree l receives contributions from $S_{gh}(l)$ in a degree range of $l \pm L_{\mathrm{win}}$ and implies that the range of spherical harmonic degrees (from $l_{\min}$ to $l_{\max}$) that can be used in the inversion is negatively correlated with L_{win} (see details in section 2.4). To ensure a wide degree range for inversion, we need to choose L_{win} as small as possible. On the other hand, L_{win} must be high enough for the localization windows to be effectively concentrated in the target cap region of a given θ_0. Our chosen L_{win} is the minimum value when at least one (and in fact only one) perfectly concentrated window
($\lambda \geq 99\%$) is available.

2.2. Global Flexural Models

We applied the thin-plate lithospheric flexural model following Turcotte et al. (1981) and McGovern et al. (2002). Here, the elastic lithosphere is approximated as a thin shell overlying an inviscid substratum (i.e., the asthenosphere); the plate flexes in response to both surface and subsurface loading. The thin-plate approximation is valid when the vertical deformation of the lithosphere is small compared to its thickness, and the lithospheric thickness is small compared to the radius of the plate bending curvature. Watts (2001) reviewed the numerical results of the more general thick-plate models by Comer (1983), Wolf (1985), and Zhou (1991) and concluded that the thin-plate model is a satisfactory approximation because it differs from the thick-plate model only in the short wavelength range that is unimportant in the *Te* inversion.

The resultant density structure due to tectonic loading and plate bending (Figure 2a) determines the gravitational signature. The theoretical admittance and correlation in the global scale take the following form:

$$Z(l) = Z_l(Te, \rho_t, f, \alpha, \ldots), \tag{6}$$

$$\gamma(l) = \gamma_l(Te, \rho_t, f, \alpha, \ldots), \tag{7}$$

where *Te* is the effective thickness of the elastic lithosphere, and ρ_t is the surface load density. Any deviation of the surface and the crust-mantle interface (black solid curves in Figure 2a) from initial flat interfaces (black dashed lines) is treated as due to surface and subsurface loading, in combination with the resultant lithospheric flexure (green dashed curves). In this model, we implicitly assumed that the subsurface loading occurs on the crust-mantle interface. Following Wieczorek (2007), loads can be described by two parameters: α is the phase difference between subsurface and surface loading, and f is the amplitude ratio of the subsurface to surface loading:

$$\alpha = \frac{\sum_{m=-l}^{l} h_{lm}^i w_{lm}^i}{\sqrt{\sum_{m=-l}^{l}\left(h_{lm}^i\right)^2}\sqrt{\sum_{m=-l}^{l}\left(w_{lm}^i\right)^2}}, \tag{8}$$

$$f = \frac{\Delta\rho_b\sqrt{\sum_{m=-l}^{l}\left(w_{lm}^i\right)^2}}{\rho_t\sqrt{\sum_{m=-l}^{l}\left(h_{lm}^i\right)^2}}, \tag{9}$$

where h_{lm}^i and w_{lm}^i are the spherical harmonic coefficients for the initial surface and subsurface loading, respectively. The loading parameters are assumed to be independent of the wavelength, and therefore the subscript l is omitted here. An α value of 0 represents the case when the subsurface and surface loads are

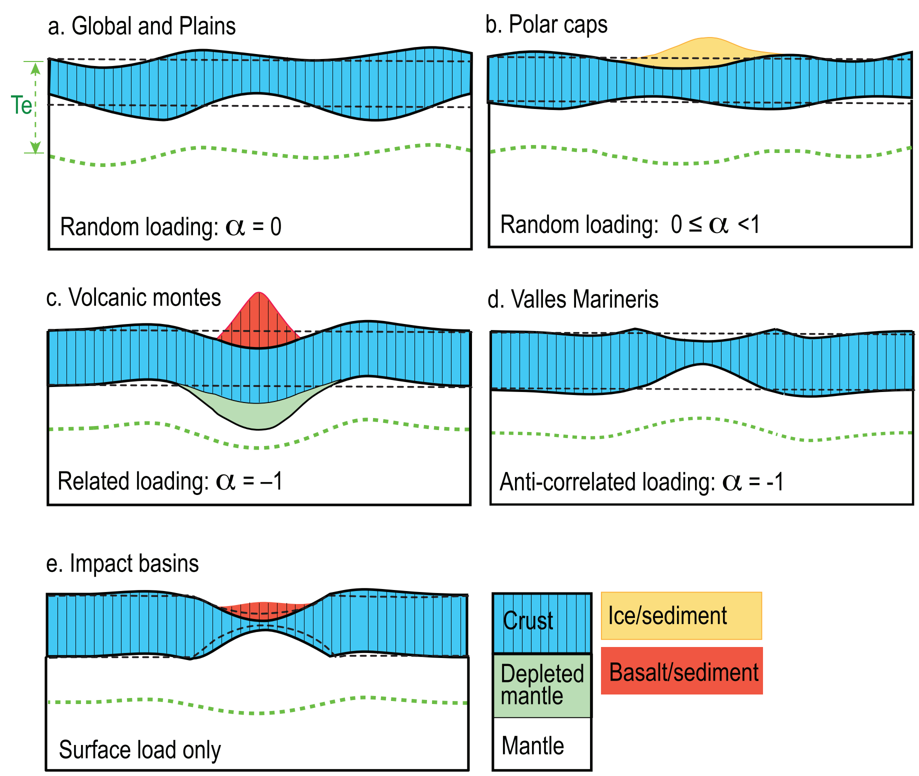

Figure 2. Cartoon illustrations of the loading types and assumed α values for (a) global model and plains, (b) polar caps, (c) volcanic montes, (d) Valles Marineris, and (e) impact basins. The blue region indicates the present crustal structure, while the underlying green region (in Panel c) and white regions indicate depleted mantle (or mantle plume) and regular mantle, respectively. The orange and red regions indicate surface loading with a density value different from the crustal density. The black dashed curves represent the initial surface and Moho relief, which are flat except for (e) impact basins, prior to tectonic loading. Deviations of the solid curves from the dashed curves are due to the tectonic loading and corresponding lithospheric flexure. Dashed green curves delineate the lithosphere flexure.

random in phase (likely due to long-term erosion and sedimentation; Forsyth, 1985; Wieczorek, 2007), while α values of 1 and -1 correspond to the cases when the subsurface and surface loads are perfectly in and out of phase, respectively. The ellipsis in equations (6) and (7) denote fixed parameters in Table 1. Among these parameters, we fixed the crustal thickness at the best fit global values of 50 km (Neumann et al., 2004; Wieczorek & Zuber, 2004; Zuber, 2001) given its less significant influence on the models (Figures S2 and S3). The crustal density was further assumed to be equal to the surface loading density for the global model.

Table 1
Fixed Parameters

Parameters	Description	Value
E	Young's modulus of elastic lithosphere (Pa)	1×10^{11}
ν	Poisson's ratio of elastic lithosphere	0.25
ρ_c	Crustal density (kg/m^3)	2,900
H_c	Crustal thickness (km)	50
z_b	Depth of subsurface loading (same as H_c) (km)	50
ρ_m	Mantle density (kg/m^3)	3,500
$\Delta\rho_b$	Density contrast of subsurface load to crust ($\rho_m - \rho_c$) (kg/m^3)	600
R_{obs}	Observational radius of Martian gravity field (km)	3,396
R	Average radius of Mars (km)	3,389.5
g	Gravity acceleration at the radius of R (m/s^2)	3.73

Details of calculations for the global thin-plate flexural models are provided in supporting information Text S1. Our global admittance and correlation models (dashed curves in Figure 3) are similar to that of Wieczorek (2007), Simons and Olhede (2013), and Kirby (2014). The theoretical admittance (Figure 3, top panels) approaches 0 in the lowest degree (reflecting local Airy isostatic compensation), while the admittance asymptotically approaches ~ $2\pi G\rho_t$ in the highest degrees (reflecting noncompensation). When Te increases, the transitional degree range of the admittance becomes narrower and shifts to lower degrees (Figure 3a). In comparison, the modeled correlation is less sensitive to Te but highly depends on f (Figure 3b). Thus, jointly inverting the admittance and correlation helps to better constrain the model parameters.

2.3. Localized Flexural Models

The above global models need to be localized before comparison with the localized observations. The large-scale topographic features of Mars fall

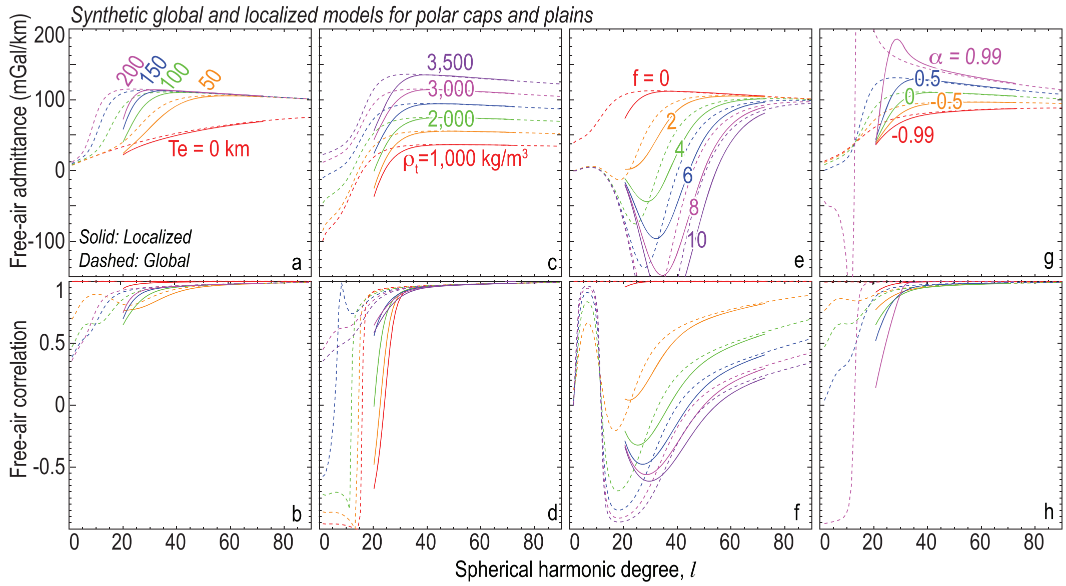

Figure 3. Theoretical admittance and correlation for a series of lithospheric flexural models: (a, b) Varied T_e, assuming ρ_t = 2,900 kg/m^3, f = 0.5, and $\alpha = 0$; (c, d) varied ρ_t, assuming T_e = 100 km, f = 0.5, and $\alpha = 0$; (e, f) varied f, assuming T_e = 100 km, ρ_t = 2,900 kg/m^3, and $\alpha = 0$; and (g, h) varied α, assuming T_e = 100 km, ρ_t = 2,900 kg/m^3, and f = 0.5. Dashed curves are global models. Solid curves are localized models assuming $S_{hh}(l)$~$l^{-2.5}$, $2\theta_o$= 30°, and L_{win} = 17, applicable to polar caps and plains.

into five distinct tectonic types: Polar regions, plains, volcanic montes, Valles Marineris, and impact basins. These five tectonic types have been shaped by different geologic processes, that is, ice deposits, erosion, volcanism, extension and rifting, and impacts, respectively. Cartoon illustrations in Figure 2 highlight these different regional tectonics and loading scenarios. Accordingly, we applied two distinct localization methods. The statistical localization method (using equation (5)) is applicable to the polar and plains regions where the surface and subsurface loading are mostly uncorrelated, while the deterministic localization method (McGovern et al., 2002) is suitable for the other tectonic subregions where surface and subsurface loading are correlated. Typical localized flexural models are shown in Figures 3–5.

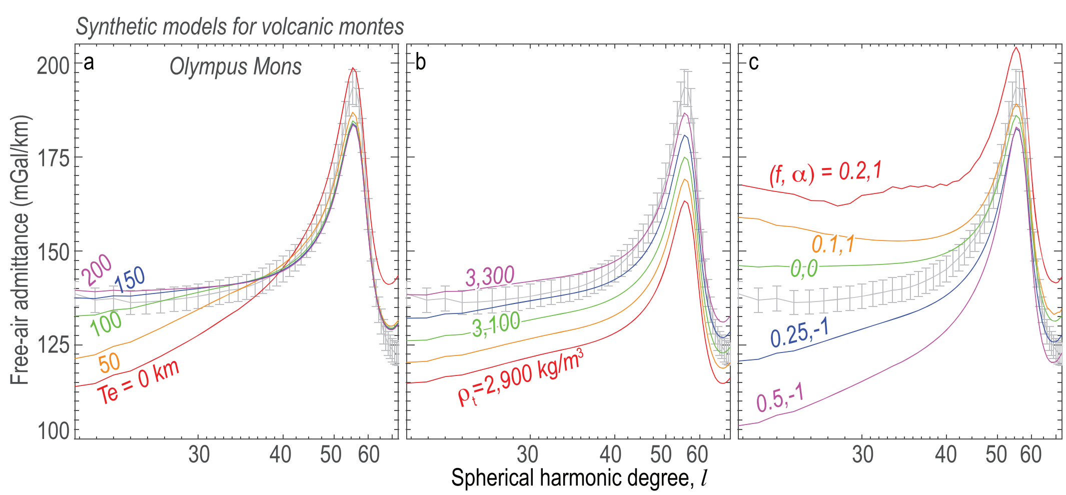

Figure 4. Theoretical admittance models (colored curves) for Olympus Mons: (a) Varied T_e, assuming ρ_t = 3,300 kg/m^3, f = 0.1, and $\alpha = -1$; (b) varied ρ_t, assuming T_e = 129 km, f = 0.1, and $\alpha = -1$; and (c) varied f and α, assuming T_e = 129 km, ρ_t = 3,300 kg/m^3. For comparison, gray curves with error bars are observed admittance.

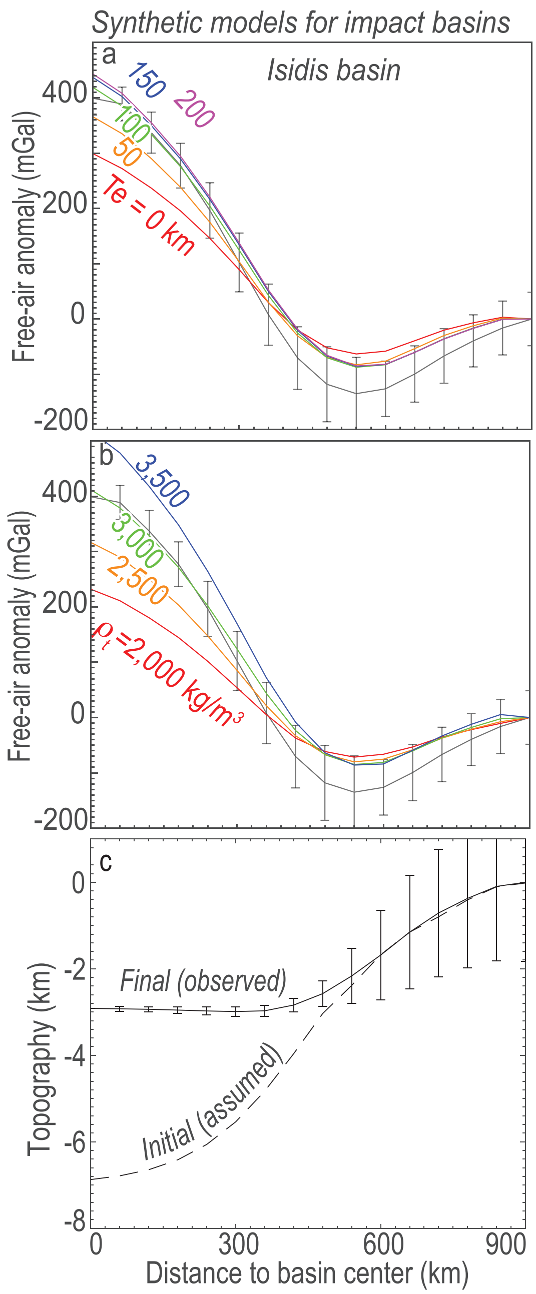

Figure 5. Theoretical gravity models (colored curves) for the Isidis basin along an azimuthally averaged profiles: (a) Varied T_e, assuming $\rho_t = 3{,}126$ kg/m^3; (b) varied ρ_t, assuming $T_e = 154$ km. Gray curves with error bars indicate the means and standard deviations of observed gravity samples taken at 1° intervals. (c) Observed topography (solid curves with error bars) and assumed pre-infill topography following a hyperbolic tangent function (supporting information Text S3).

2.3.1. Plains

This first tectonic type is widespread on Mars in both the more densely cratered southern hemisphere and the more sparsely cratered northern hemisphere. The southern plains are mostly Noachian in age, while the northern plains are Hesperian to Amazonian. The loading scenario and lithospheric strength of the plains thus provide vital clues to the formation and evolution of the hemispheric dichotomy. Forsyth (1985) suggested that erosion processes randomize the surface and subsurface loading in the plains (Figure 2a), and erosion has certainly been an active process on Mars. We can thus reasonably assume α to be ~ 0 and used equation (5) to convert global spectral models to localized spectral models (see details in supporting information Text S2). Figure 3 shows that the localization (solid curves) systematically reduces the global spectral models (dashed curves) in the low degrees. By comparing localized models with observed spectra, we then inverted for three parameters, that is, Te, ρ_t, and f. For the northern plains, the observed high admittance and low correlation cannot be well fit by $\alpha = 0$. We thus considered a second model in which the phase parameter α was inverted simultaneously. We assumed the crustal density to be equal to ρ_t with a permitted range of 2,200–3,300 kg/m^3. The lower bound corresponds to sedimentary rocks (Zuber et al., 2000) and the upper bound to basaltic shergottites (Baratoux et al., 2014).

2.3.2. Polar Regions

The northern and southern polar caps on Mars are reservoirs of multikilometer-thick layered deposits of dusty water ice (yellow region in Figure 2b; Byrne, 2009) under residual ice caps of a few meters thick. These layered deposits are young geologic features (late Amazonian, <100 Ma) that change in volume due to climate variations and the Milankovitch cycle on a timescale of ~0.1–1,000 Ma. The Martian mantle is expected to respond to the changing polar layered deposits viscously on a similar timescale. This viscous response has been suggested to cause the poor correlation between the gravity and topography (e.g., Johnson et al., 2000). We modeled the current polar layered deposits as surface loading. At the same time, we modeled the undulations of the crust-mantle interface due to earlier polar ice deposits as subsurface loading (Figure 2b), because the earlier polar ice deposits are no longer directly observable in the topographic data. We first assumed an a priori ρ_t range of 1,000–2,000 kg/m^3, corresponding to mixtures of ice and sediments (e.g., Johnson, 2000; Li et al., 2012). However, radar sounding data suggest that the polar layered deposits are almost pure water ice with a dust contamination ratio (by volume) of less than 10% (Byrne, 2009; Picardi et al., 2005; Plaut et al., 2007), corresponding to ρ_t of close to 1,000 kg/m^3. We thus considered a second model that assumes a constant ρ_t and inverted for the rest of parameters, Te, f, and α, for the two polar regions.

2.3.3. Volcanic Montes

Most of the volcanic montes on Mars are located in the Tharsis volcanic province that was mostly developed during the Noachian period (Carr & Head, 2010; Phillips et al., 2001); reduced volcanic activities might have continued into the Hesperian and Amazonian, as suggested by the surface ages of volcanic montes (Table 2). We also investigated Elysium Mons that is outside the Tharsis province.

The volcanic edifice is commonly accompanied by complex subsurface loading structures, such as dike intrusions and depleted mantle residuals. The coexistence and simultaneous formation of the surface and subsurface loading imply that they are highly (anti)correlated (α ~ ±1). All the volcanic montes show a gravity/topography correlation close to 1, which is also consistent with α ~ ±1 (Belleguic et al., 2005;

Table 2
Feature Locations, Localization Windows, and Surface Loading Ages

Tectonic type	Feature	Latitude (°)	Longitude (°)	$2\theta_o$ (°)	L_{win}	Loading age[a]
Polar caps	Northern pole	90	0	20	26	lA
	Southern pole	−89	165	20	26	lA
Southern plains	Arabia Terra	30, 25, 10	20, 0, 0	30	17	N
	Noachis Terra	−30, −60, −30, −60	15, 15, −15, −15	30	17	N
	Terra Cimmeria	−15, −45, −30, −50	135, 135, 165, 165	30	17	N
	Terra Sirenum	−30, −50, −50	195, 195, 220	30	17	N
Volcanic plains	Solis Planum	−25	270	30	17	H
Northern plains	Vastitas Borealis	65, 65, 65, 65	30, 60, 180, 300	30	17	HA
	Acidalia Planitia	46.7, 50	338, 350	30	17	H
Volcanic montes	Olympus Mons	19	226.5	30	17	HA
	Alba Mons	42	249	30	17	HA
	Elysium Mons	25	147	30	17	H
	Arsia Mons	−9	239	20	26	HA
	Pavonis Mons	0.5	247	20	26	HA
	Ascraeus Mons	11.5	256	20	26	HA
Rift Valley	Ius Chasma	−8.3	280	20	26	HA
(Valles Marineris)	Melas Chasma	−11.5	290.3	20	26	HA
	Coportates Chasma	−13.8	301.4	20	26	HA
Impact basins	Utopia basin	42	114	50	11	NH
	Isidis basin	12	87	30	17	NHA
	Argyre basin	−49.7	316	30	17	NH

[a]Loading ages are from Thomson and Head (2001), Werner (2008), Ivanov et al. (2012), and Dohm et al. (2015) for the impact basins; Werner (2009) for volcanoes; and Tanaka et al. (2013) for other regions. N, H, and A refer to Noachian, Hesperian, and Amazonian periods, respectively, and l is short for late.

Beuthe et al., 2012 ; McGovern et al., 2002). We applied the deterministic method of McGovern et al. (2002): For a given set of model parameters, the observed topography was first inverted for the surface and subsurface loading distribution in the spatial domain, and then the corresponding gravity fields were forward modeled. The modeled gravity fields were then localized and combined with observed topography to yield localized admittance models. The surface and subsurface loading distribution is uniquely determined as they are assumed to be fully correlated ($\alpha = 1$) or anticorrelated ($\alpha = -1$).

This deterministic method also permits the incorporation of nonlinear finite-amplitude correction in calculating gravitational signals of the topographic density interface. The finite-amplitude correction is critical for the volcanic montes, especially for Olympus Mons (due to its large topographic curvature), which has a spectral peak in the degree range of 40–60 (Figure 4) (Beuthe et al., 2012; McGovern et al., 2002). This finite-amplitude correction is negligible for the other tectonic types. We improved upon the analysis of McGovern et al. (2002) and expanded the usage of their codes from the original model of dense subsurface intrusion ($\alpha = 1$) to an additional model of buoyant subsurface loading (Figure 2c, $\alpha = -1$, due to a mantle plume and/or depleted mantle composition; Belleguic et al., 2005; Beuthe et al., 2012). In practice, we inverted for three parameters (Te, ρ_t, and αf), and αf was allowed to be both positive and negative. Figure 4 shows the model sensitivity to Te, ρ_t, and f for Olympus Mons. We assumed the a priori ρ_t range for the volcanic montes to be 2,900–3,300 kg/m^3. This density range is based on a measured pore-free grain density of 3,100–3,600 kg/m^3 for igneous rock measurements at Gusev crater (Baratoux et al., 2014), assuming a rock porosity of 10% (Britt & Consolmagno, 2003) and that the porosity space is filled with water.

2.3.4. Valles Marineris

This prominent 4,000-km-long rift valley system lies in the southeast of the Tharsis province and stretches for nearly a quarter of the planet's circumference. This system formed in the Hesperian to Amazonian due to tectonic extension and rifting. We expected the co-existence of negative surface loading and positive subsurface loading (due to rift-induced crustal thinning or high-density dike intrusions, Figure 2d), and therefore set $\alpha = -1$ (McGovern et al., 2002). We further assumed the crustal density to be equal to ρ_t with a permitted range of 2,200–3,300 kg/m^3. We selected three segments, Ius, Melas, and Coprates Chasma, to investigate the lithospheric and loading variations.

2.3.5. Impact Basins

Major impact basins on Mars include the Isidis, Argyre, Hellas, and Utopia basins. Those impact basins are thought to have formed during the Noachian period, followed by long-term sediment or mare basalt loading in the Hesperian or Amazonian (Tanaka et al., 2013; Werner, 2009). Different from the loading scenarios for the previous four tectonic types, the initial surface and Moho relief (dashed curves in Figure 2e) of the impact basins were not flat prior to the (surface) loading. We quantified the initial topographic depression based on the empirical crater depth-diameter power law relationship for Martian fresh impact craters (Howenstine & Kiefer, 2005) and an assumed axisymmetric hyperbolic tangent function (e.g., dashed curve in Figure 5c; see supporting information Text S3 for details). We further assumed that the initial free-air gravity is negligible due to the Airy isostatic state and the existence of an uplifted mantle plug (Neumann et al., 2004; Searls et al., 2006). Our method of modeling the gravitational signature is similar to the deterministic method of McGovern et al. (2002) for the volcanic montes except that we took into account the initial topographic depression and mantle plug here (Figure 2e). We permitted a ρ_t range of 2,200–3,300 kg/m^3 because the surface loading could be sedimentary or volcanic (e.g., Dohm et al., 2015; Ivanov et al., 2012; Thomson & Head, 2001). We found significant misfits between the observations and models in the spectral domain for all three basins (Figure S5), suggesting that unmodeled anisotropy in the pre-infill state and/or surface loading might be essential. We thus present spatial inversion results for the impact basins. To eliminate the effect of azimuthal anisotropy, we azimuthally averaged the gravity signatures from the basin center to one basin radius (Figure 5 for the Isidis basin). The colored curves in Figures 5a and 5b show the model sensitivity to Te and ρ_t.

2.4. MCMC Method

We applied the MCMC method (Smith, 2013) to obtain the posterior distribution of parameters, as described in detail in supporting information Text S4. We sampled the parameter space $X^i = \left(Te^i, \rho_t^i\right)$, $\left(Te^i, \rho_t^i, f^i/\alpha f^i\right)$, or $\left(Te^i, \rho_t^i, f^i, \alpha^i\right)$ by the MCMC approach with the adaptive Metropolis (AM) algorithm of Haario et al. (2001). For a Markov chain X^i, relative to the previous sample, the next sample always has an equal or higher posterior probability to fit the observation. We used a coarsened posterior distribution to estimate the posterior probability:

$$P_\beta\left(X^i | Z^{\text{obs}}(l), \gamma^{\text{obs}}(l)\right) \propto P\left(X^i\right) P\left(Z^{\text{obs}}(l), \gamma^{\text{obs}}(l) | X^i\right)^{\frac{1}{\beta}}, \tag{10}$$

where $P(X^i)$ is a uniform prior distribution ensuring X^i within the a priori ranges, which were assumed to be different for each tectonic type (section 2.3). The posterior likelihood $P(Z^{\text{obs}}(l),\gamma^{\text{obs}}(l)| X^i)$ was assumed to take an exponential form of the chi-square function $\chi^2(X^i)$, assuming that the observational errors follow independent Gaussian distributions with standard deviations of $\sigma_Z^{\text{obs}}(l)$ and $\sigma_\gamma^{\text{obs}}(l)$ (equations (3) and (4)):

$$P\left(Z^{obs}(l), \gamma^{obs}(l) | X^i\right) \propto \exp\left(-\frac{\chi^2\left(X^i\right)}{2}\right), \tag{11}$$

$$\chi^2\left(X^i\right) = \sum_{l=l_{\min}}^{l_{\max}} \left(\frac{Z^{\text{model}}\left(l, X^i\right) - Z^{\text{obs}}(l)}{\sigma_Z^{\text{obs}}(l)}\right)^2 + \left(\frac{\gamma^{\text{model}}\left(l, X^i\right) - \gamma^{\text{obs}}(l)}{\sigma_\gamma^{\text{obs}}(l)}\right)^2, \tag{12}$$

where the second term in equation (12) should be eliminated when only the admittance is used for volcanic montes and Valles Marineris.

The coarsening for the posterior distribution in equation (10) is necessary to reduce the problem of uncertainty underestimation due to model misspecification (Gu et al., 2018; Miller & Dunson, 2019). The choice of the coarsening parameter β greatly influences the posterior range of the accepted admittance and correlation models (e.g., Figure S6). When $\beta = 1$, the posterior probability becomes the standard Bayes' Formula without coarsening. In this situation, the MCMC chain concentrates on narrower acceptable ranges than expected, and the corresponding model uncertainties are underestimated (comparing the red and black

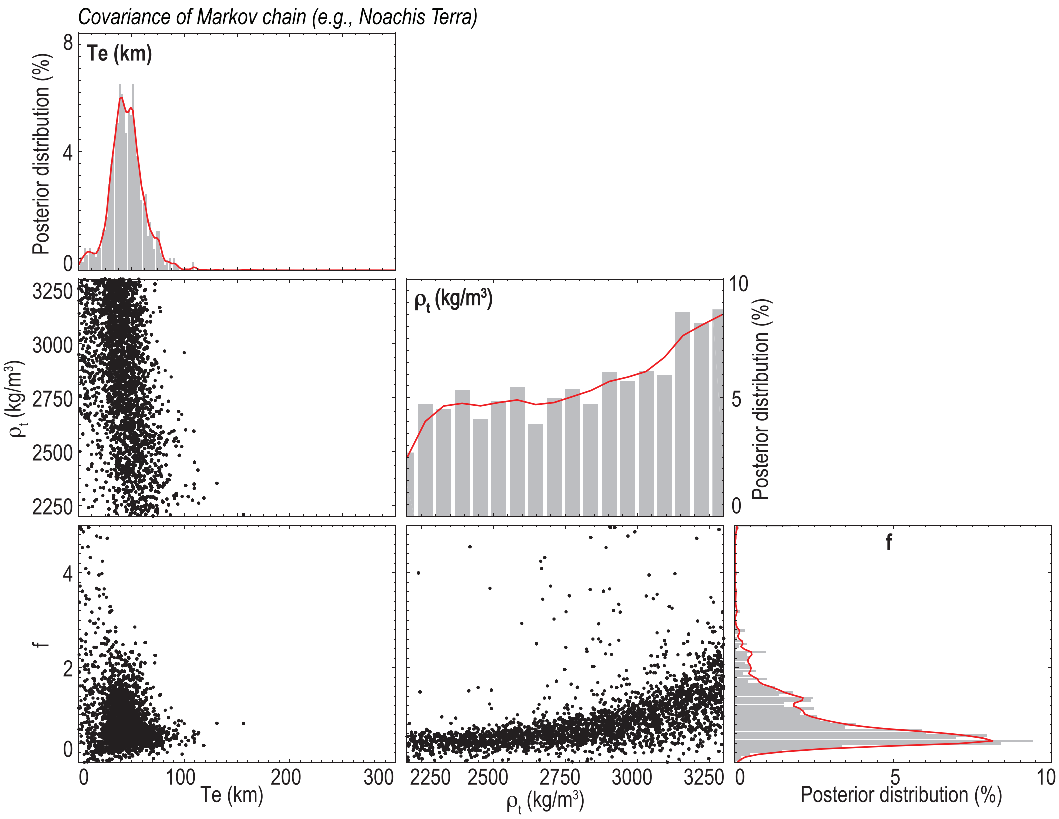

Figure 6. Scatter plots and histograms of the joint Markov chains $X^i = \left(Te^i, \rho_t^i, f^i\right)$ for Noachis Terra (with corresponding admittance and correlation in Figure 7c and 7d). Superimposed red curves indicate continuous probability density functions to fit the histograms.

error bars in Figures S6a and S6b). A larger β is thus required to down weight the posterior likelihood in order to quantify the model uncertainty correctly (Figures S6c–S6f). For each subregion, we solved for the best β value that keeps the mean posterior range of the admittance and correlation to be equal to the mean observational error. The tested β values varied from 1 to 40 with a stepping of 5. Figure S7 shows a typical figure to choose the β value, yielding a best value of 15. Table S1 lists our chosen β values for different subregions.

The choice of degree range of $l_{\min}$ to $l_{\max}$ (Table 2) for fitting was based on visual inspection as well as trial and error to ensure that within the chosen degree range the observed spectra are explainable by our uniform-parameter models (see the next paragraph). The chosen $l_{\max}$ must be lower than 90–L_{win} to avoid the effects of high-degree observational errors in the gravity model. Similarly, the chosen $l_{\min}$ must be larger than $L_{\text{win}} + 5$ to avoid bias caused by degree 2–4 features (Figure S1) likely due to mantle convection (Zhong, 2002; Zhong & Zuber, 2001). For the spatial analysis of the three impact basins, we replaced the admittance and correlation spectra by the control points of the azimuthally averaged gravity profiles. In practice, a coarsened marginal probability distribution is necessary in the construction of a Markov chain to reduce the problem of uncertainty underestimation due to model misspecification (details in supporting information Text S4).

An underlying assumption for our inversion is that all the model parameters are degree independent. If the model parameters are instead allowed to vary as a function of spectral degree l, the number of free parameters to solve would increase rapidly and become unconstrained. Therefore, in this study we focused on end-member models by searching for a set of uniform model parameters that could best fit the observations of all degrees (hereafter referred to as "uniform-parameter models"). However, in reality, a substantial

Table 3
Estimated Flexural Parameters

Feature	*l* range for fitting	α Range	α Best fit	*Te* (km) Range	*Te* (km) Best fit	ρ_t (kg/m^3) Range	ρ_t (kg/m^3) Best fit	f Range	f Best fit	NRMSE	Previous *Te* (km)
Northern pole	31–48	0[a]		>150	225	1,350–1,800	1,650	0.4–0.5	0.4	0.81	60–120[b], >300[c]
		0.3–0.5	0.4	>190	240	1,000[a]		2.0–2.9	2.3	0.98	
Southern Pole	35–45	0[a]		>85	265	<1,400	1,110	0.2–0.3	0.3	1.10	>102[d], >150[e]
		0–0.3	0.2	>185	255	1,000[a]		0.8–1.3	1.0	1.08	
Arabia Terra	22–30	0[a]		NC	60	NC	3,300	0.7–3.8	0.8	0.33	<16[f]
Noachis Terra	22–44	0[a]		30–60	40	NC	3,300	0.4–1.4	0.4	0.71	<12[f]
Terra Cimmeria	22–30	0[a]		20–35	35	NC	3,200	<2.1	0.2	1.06	<20[f]
	41–73	0[a]		25–50	30	NC	3,300	0.9–3.3	1.0	0.52	
Terra Sirenum	22–33	0[a]		35–50	40	NC	3,300	0.3–1.3	0.4	1.44	
Solis Planum	22–37	0[a]		60–95	70	>3,000	3,300	1.0–2.0	1.1	1.34	24–37[f]
Vastitas Borealis	22–45	0[a]		>140	300	NC	3,200	2.2–9.2	2.8	0.89	
	22–45	−0.1 to 0.6	0.5	>135	270	NC	3,300	2.5–13	3.4	0.63	
Acidalia Planitia	22–28	0[a]		>105	270	NC	3,100	2.6–11	3.4	1.18	<45[g]
	37–51	0[a]		>115	260	NC	2,850	4.4–12	5.5	1.22	
	22–28	> − 0.5	1	>115	300	NC	3,300	2.9–12	3.3	0.91	
	37–51	−0.1 to 0.4	0.2	90–210	120	NC	2,400	4.1–12	11.4	0.68	
Olympus Mons	22–73	±1[a]		>105	300	>3,100	3,300	−0.1 to 0[h]	−0.1	1.25	>70[i], >150[j]
Alba Mons	22–35	±1[a]		60–210	75	NC	3,300	−0.5 to −0.2[h]	−0.4	1.25	43–103[i], 0[k]
Elysium Mons	22–40	±1[a]		<55	15	>3,200	3,300	−0.1 to 0[h]	0	1.71	<175[i]
Arsia Mons	31–64	±1[a]		<15	10	>3,250	3,300	−0.1 to 0[h]	−0.1	0.8	<35[i]
Pavonis Mons	31–35	±1[a]		NC	175	>3,200	3,300	0–0.1[h]	0	0.49	>50[i]
	47–64	±1[a]		<15	0	>3,250	3,300	−0.3 to 0[h]	−0.1	1.29	<40 [k]
Ascraeus Mons	31–41	±1[a]		>90	95	>3,150	3,300	−0.1 to 0[h]	0	0.65	>50[i]
Ius Chasma	32–51	−1[a]		>105	115	>2,550	3,050	0.2–0.8	0.7	0.39	>80[k]
Melas Chasma	31–39	−1[a]		>150	300	<2,800	2,250	0.2–0.6	0.3	1.29	>110[k]
	40–64	−1[a]		>55	65	2,650–3,100	3,000	0.5–0.9	0.8	0.39	
Coprates Chasma	31–37	−1[a]		>130	230	>2,600	2,750	0.1–0.4	0.1	0.83	
	38–64	−1[a]		>130	300	2,450–2,700	2,450	0–0.3	0	0.91	
Utopia basin	Spatial	NA		<50	30	2,850–3,000	2,950	N/A	N/A	0.38	NC[l]
Argyre basin	Spatial	NA		50–130	90	<2,900	2,650	N/A	N/A	1.04	
Isidis basin	Spatial	NA		>100	300	>2,750	3,200	N/A	N/A	0.34	100–180[m]

[a]The values here are assumed (section 2.3). [b]Johnson et al. (2000). [c]Phillips et al. (2008). [d]Wieczorek (2008). [e]Plaut et al. (2007). [f]McGovern et al. (2004). [g]Hoogenboom and Smrekar (2006). [h]Range and best fit values are for αf. Negative sign indicates $\alpha < 0$. [i]Belleguic et al. (2005). [j]Comer et al. (1985). [k]Beuthe et al. (2012). [l]Searls et al. (2006). [m]Ritzer and Hauck (2009).

number of the observations cannot be explained by such uniform-parameter models (e.g., compare the observed spectra in Figure 7 with models in Figure 3). This is likely due to multiple loading stages that cannot be explained by a single set of parameters for one loading stage. In the following inversion for each subregion, we only used a specific degree range of the observations as constraints, for which best fitting solutions of uniform parameters might exist.

The statistics of a well-mixed Markov chain X^i were used in parameter estimation. In practice, we fitted the sample histogram by a continuous probability density function (e.g., diagonal panels in Figure 6) based on normal kernel functions; we used the mode of this probability density function to infer best fit parameter values. We then obtained the 68% confidence intervals of the sampled parameters by 16th and the 84th percentiles of the posterior samples. The presented best values and acceptable ranges of Te, ρ_t, f, and α (Table 3) were rounded to the nearest multiples of 5 km, 50 kg/m^3, 0.1, and 0.1, respectively, to match the expected precision of these inverted parameters (e.g., McGovern et al., 2002; McKenzie et al., 2002). These confidence intervals are more robust and reliable than the single best fit values because the Gaussian distribution assumption for the admittance and correlation errors is invalid (Beuthe et al., 2012; Simons & Olhede, 2013). To facilitate a comparison with previous analyses of McGovern et al. (2002), Belleguic et al. (2005), Beuthe et al. (2012), and Audet (2014), the normalized root-mean-square misfits (NRMSE) of our best fitting models are listed in Table 3.

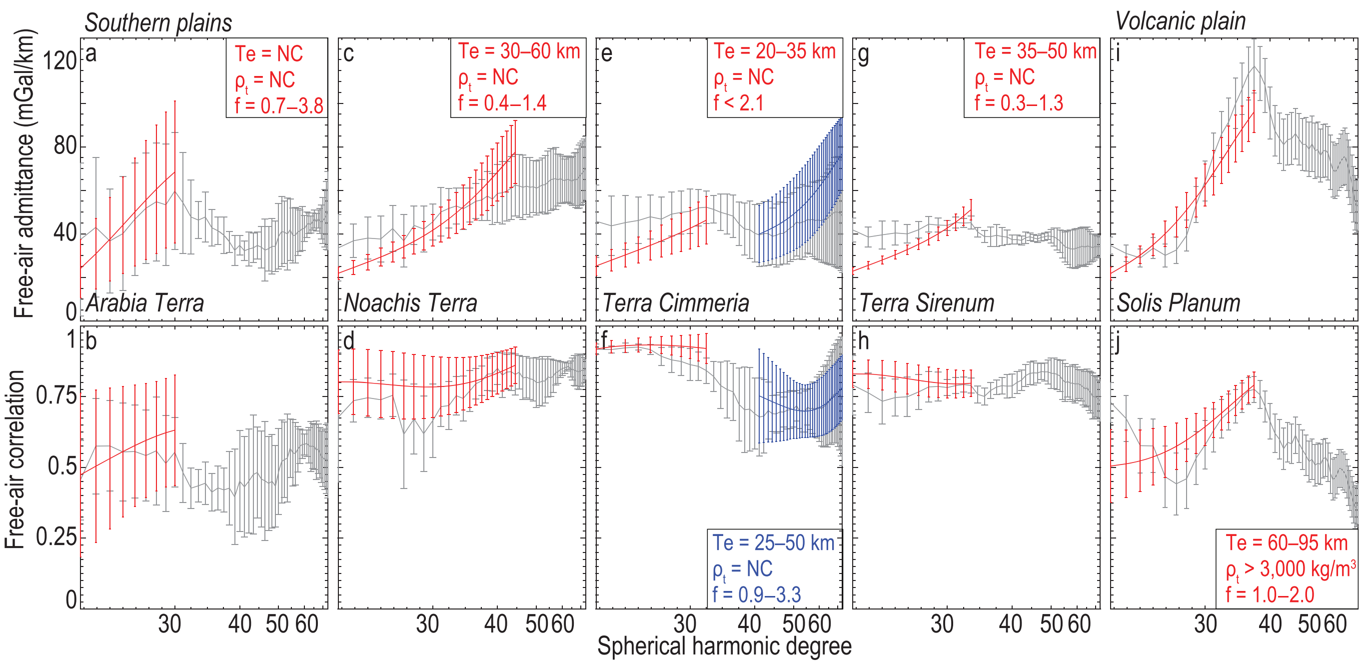

Figure 7. Comparisons between observed spectra (gray) and accepted models (red) for southern plains, including (a, b) Arabia Terra, (c, d) Noachis Terra, (e, f) Terra Cimmeria, and (g, h) Terra Sirenum, as well as a volcanic plain (i, j) Solis Planum. Gray error bars are observational errors, and red error bars are standard deviations (corresponding to 68% confidence intervals) of the accepted models. Degree ranges of the red curves indicate the selected degree ranges for fitting (Table 2). Acceptable parameter ranges for Te, ρ_t, and f are listed in red text (same as in Table 3). Blue curves and parameter ranges in (e, f) correspond to an additional flexural model for the higher degree range of Terra Cimmeria.

3. Results and Implications

We present the best fit values and acceptable ranges of Te, ρ_t, and f (and α for the northern plains and polar caps) for the selected degree (l) ranges in the 21 subregions of five distinct tectonic types in Table 3. The centers, diameters, and bandwidths (L_{win}) of the localization windows are listed in Table 2. The model fitting can be verified by comparing observations with models in Figures 7–12 and by the closeness of the NRMSE values to 0 (Table 3). The corresponding scatter plots and histograms for these solutions (similar to Figure 6) are provided in Figures S9–S38.

It is necessary to choose different degree ranges for fitting, because the uniform-parameter models cannot explain the observed admittance and correlation spectra for all degrees (e.g., Figure 7). For five subregions, we present results for two degree ranges when possible (e.g., Figures 7e and 7f). The relative magnitude of the inverted parameters for the subregions of the same tectonic type are robust (e.g., our estimated Te range of >105 km for Olympus Mons is systematically larger than the range of <55 km for Elysium Mons); meanwhile, the relative magnitudes for different tectonic types are robust only if the assumed loading scenarios represent a realistic description of reality (e.g., our estimated Te range of >105 km for Olympus Mons is larger than that of 20–60 km for the southern highlands). The inverted parameters are also expected to be dependent on the chosen degree ranges for fitting; our chosen degree ranges (Table 3) overlap notably among the investigated subregions, providing confidence that the inverted results are comparable. We also compare the inverted parameters with previous studies and discuss the geologic implications.

3.1. Plains

Among the investigated plains, we obtain systematically lower Te and f values for the four Noachian southern plains (Figure 7) than for the two Hesperian northern plains (Figure 8). For the four southern plains (Figure 7), the observed admittance spectra are <100 mGal/km, and thus we find a relatively low combined Te range of 20–60 km (Table 3). This Te range is larger than the previous estimates of <20 km by Zuber et al. (2000), McKenzie et al. (2002), and McGovern et al. (2004). The difference is mainly due to our inclusion of

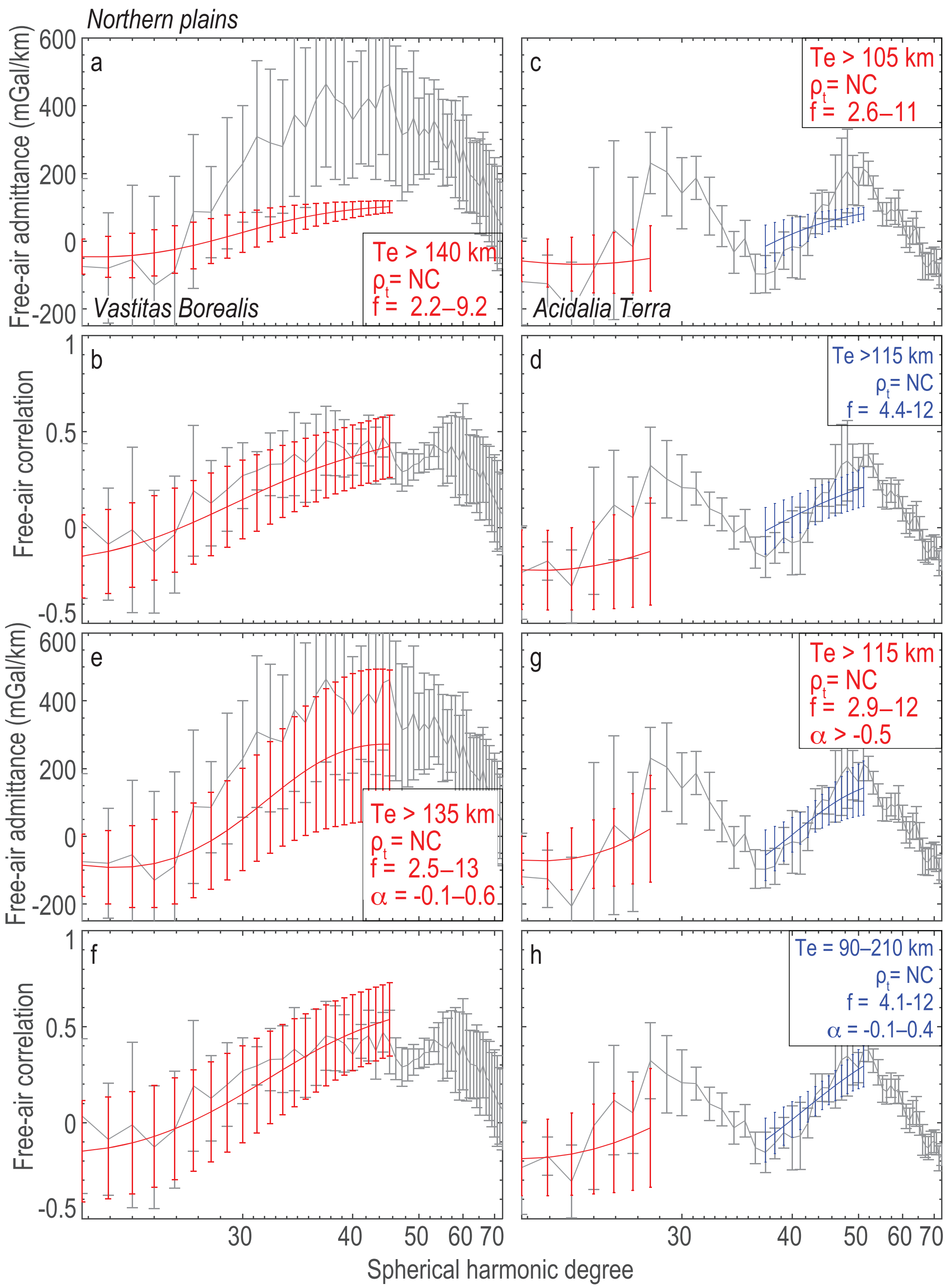

Figure 8. Comparisons between observed spectra (gray) and accepted models (red) for two northern plains: (a, b, e, f) Vastitas Borealis and (c, d, g, h) Acidalia Terra. The top two panels correspond to solutions for three varied parameters *Te*, ρ_t, and *f*, assuming $\alpha = 0$. The bottom two panels correspond to solutions for all the four parameters including α. A comparison between (a, b) and (e, f) shows a notable improvement in model fitting when α is not equal to 0.

subsurface loading that is assumed to be uncorrelated with the surface loading. The parameter ρ_t for the southern plains is not well constrained because of large observational errors of ~20 mGal/km in admittance and ~0.2 in correlation (error bars in Figure 7). The combined *f* range for the four southern plains is <3.8.

10.1029/2019JE005937

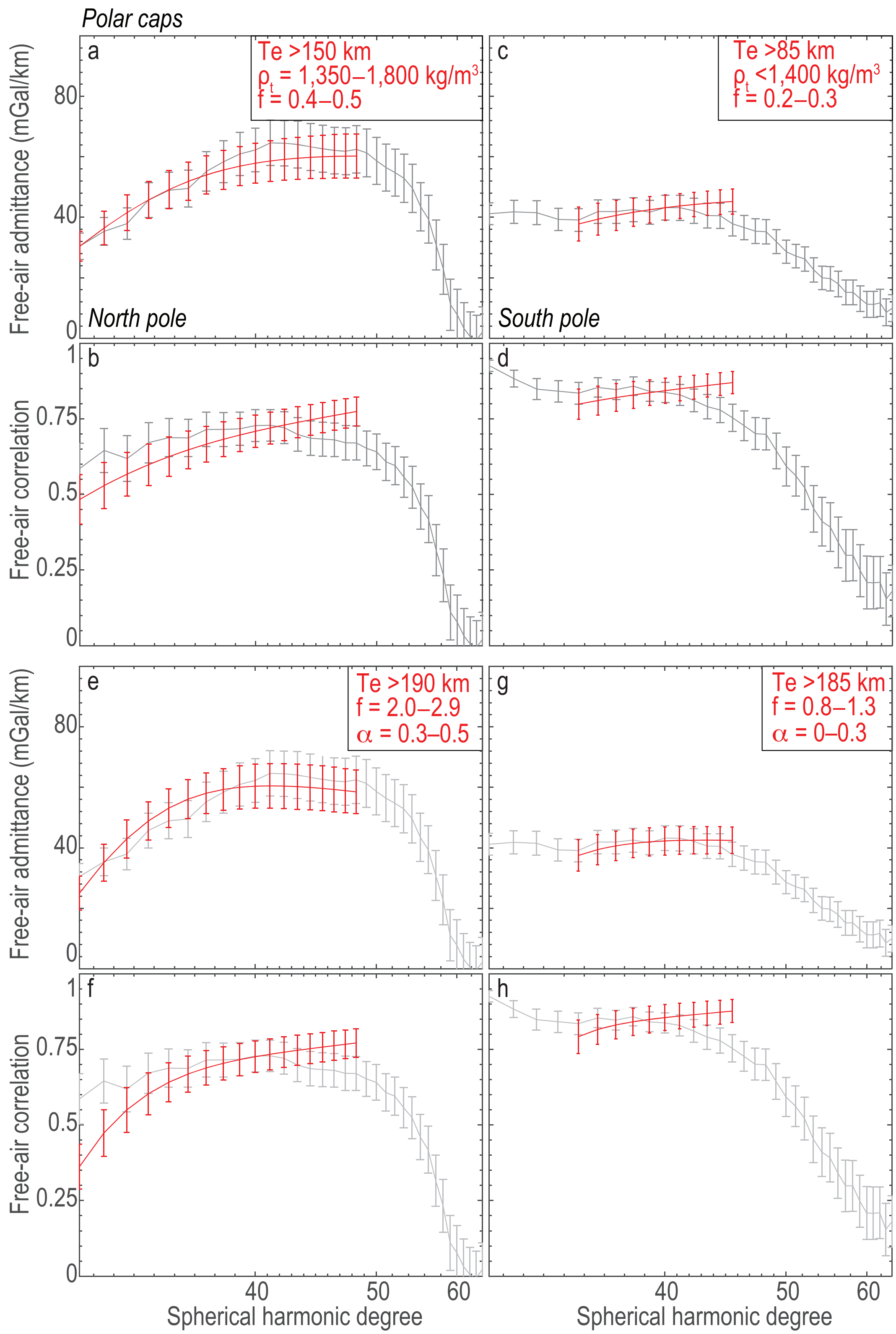

Figure 9. Comparisons between observed spectra (gray) and accepted models (red) for polar regions: (a, b, e, f) northern polar cap and (c, d, g, h) southern polar cap. The top two panels correspond to solutions for three varied parameters Te, ρ_t, and f, assuming $\alpha = 0$. The bottom two panels correspond to solutions for Te, f, and α, assuming $\rho_t = 1{,}000$ kg/m^3.

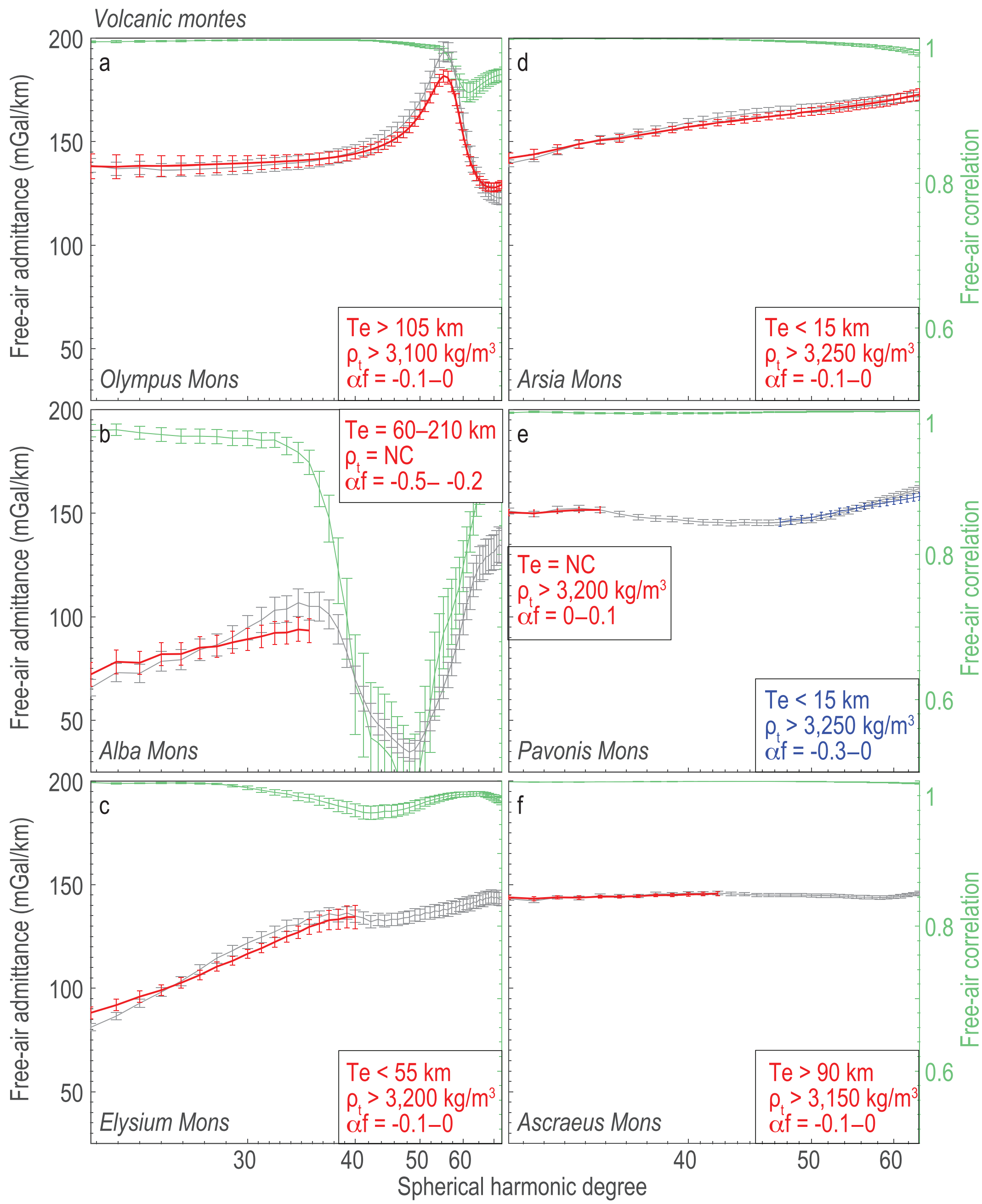

Figure 10. Comparisons between observed admittance spectra (gray) and accepted models (red) for volcanic montes when only admittance spectra are used in the inversion: (a) Olympus Mons; (b) Alba Mons; (c) Elysium Mons; (d) Arsia Mons; (e) Pavonis Mons; and (f) Ascraeus Mons. The corresponding observed correlation spectra are shown in green (right *y* axis).

The two northern plains, Vastitas Borealis and Acidalia Terra (Figure 8), show significantly larger admittance with a maximum value of ~400 mGal/km and greater fluctuations than the southern plains. Subdued and even negative correlation spectra were observed. Under the same assumption of $\alpha = 0$ with the four southern plains, we find a notably larger *Te* range (>105 km) and ƒ range (2–12) for the northern plains than for the southern plains (Figures 8a–8d). The wide parameter ranges are due to a notable parameter trade-off: Higher *Te* in combination with lower ƒ and ρ_t can fit the data equally well. We find that

10.1029/2019JE005937

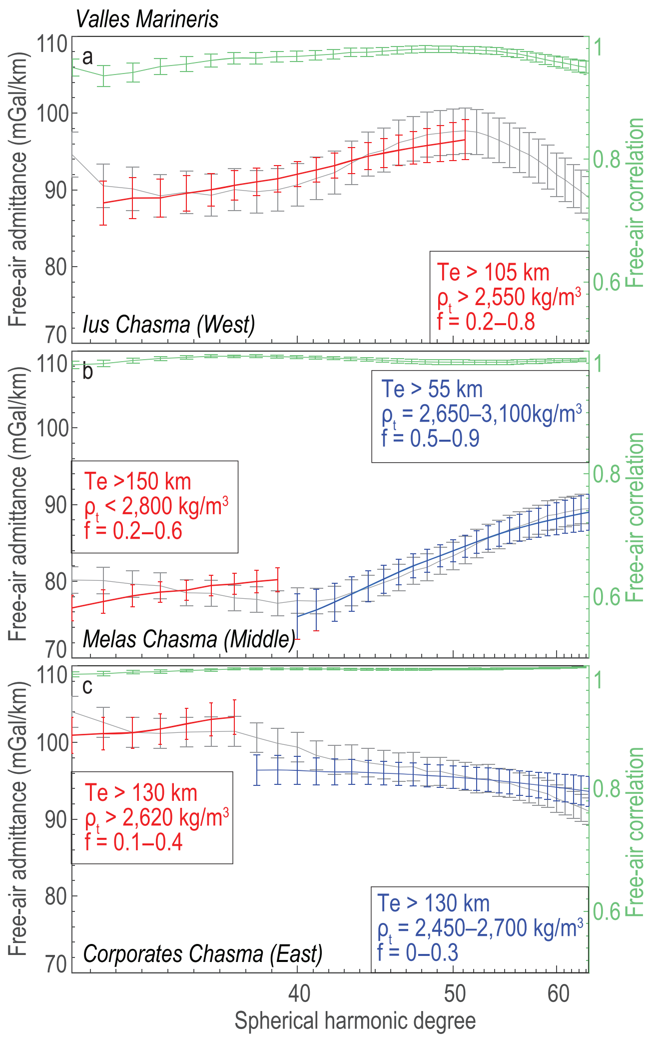

Figure 11. Comparisons between observed admittance spectra (gray) and accepted models (red) for Valles Marineris: (a) Ius Chasma (a western segment), (b) Melas Chasma (a middle segment), and (c) Coprates Chasma (an eastern segment). Blue curves and parameter ranges correspond to additional flexural models for the higher degree ranges. The corresponding observed correlation spectra are shown in green (right *y* axis).

the misfits between the observations and models are large even for the best fit models for Vastitas Borealis (Figure 8a). Letting α be a variable and inverting for it simultaneously with the other three parameters, we estimate an α range of −0.1 to 0.6 that can better explain the observed free-air admittance in Vastitas Borealis (Figure 8e). This α range, in combination with our estimated f range of 2.5–13.2, implies that the subsurface loading overwhelms the surface loading with nonnegligible correlation between the surface and subsurface loading.

The subsurface loading in the northern plains may correspond to ancient buried features, either as mantle plumes (Zhong & Zuber, 2001) or buried impact basins (Frey et al., 2001; Watters et al., 2006). After the formation of the northern lowland basement (i.e., Borealis basin) in the early Noachian period, most likely due to a giant impact (Andrews-Hanna et al., 2008; Marinova et al., 2008; Wilhelms & Squyres, 1984), long-term erosional, sedimentary, and magmatic processes flattened the ancient topography. These long-term tectonic loading processes, mostly in the Hesperian period, induce a positive correlation (i.e., $\alpha > 0$) between the surface and subsurface loading (McKenzie, 2003, 2016). Hoogenboom and Smrekar (2006) found that four specific northern plain regions with low and smooth admittance can be explained by a very low *Te* of <45 km, assuming subsurface loading only. Their *Te* range corresponds to a synchronous formation of the northern lowland basement with the southern highlands in the Noachian period, which is compatible with the giant impact origin of the Borealis basin. In contrast, our analyses consider the subsequent long-term tectonic loading processes, and our larger *Te* estimates are consistent with lower heat flux in the Hesperian period.

For the Hesperian volcanic plain, Solis Planum (Figures 7i and 7j), we estimate *Te* to be 60–95 km, greater than the range of 24–37 km estimated by the admittance analysis of McGovern et al. (2004) without considering subsurface loading. Our estimated f range of 1–2 indicates a significant amount of subsurface loading (possibly in the form of dike intrusions) that may overwhelm the surface loading. Our estimated ρ_t of >3,000 kg/m^3 implies high-density materials with a volcanic origin.

3.2. Polar Caps

Our estimated *Te* ranges for the two polar caps (Figure 9) are the largest among all of our investigated tectonic types. We excluded the high-degree ranges for fitting, because the observed reduction in the high-degree ranges could be due to a lack of resolution in the gravity data and cannot be explained by uniform-parameter models. The existence of subsurface loading is necessary to explain the observed deviations of the correlation spectra from 1.

Our inversion results show that the greater admittance spectra for the north pole requires either a larger ρ_t (Figure 9a) or α (Figure 9e) than the south pole (Figures 9c and 9g). The former (larger ρ_t) implies a higher sediment/ice ratio or denser sediment component for the north polar layered deposits (i.e., surface loading), while the latter (larger α) implies a higher degree of correlation between the surface and subsurface loading. The former explanation of larger ρ_t is less likely, because radar sounding data suggest a very low dust content of less than 2% for the north polar layered deposits (Picardi et al., 2005), and the expected mean density of the polar deposits cannot exceed 1,100 kg/m^3 even if a high-density basal unit (Byrne, 2009; Byrne & Murray, 2002) is considered. In the latter explanation of larger α, the subsurface loading might be related to the earlier depression of the crust-mantle interface when the polar ice cap had a larger extent (Fishbaugh & Head, 2005). In addition, the larger α and f estimates for the northern polar cap imply its larger deviation from a steady state, likely due to its younger age than the southern polar cap (Fishbaugh & Head, 2001).

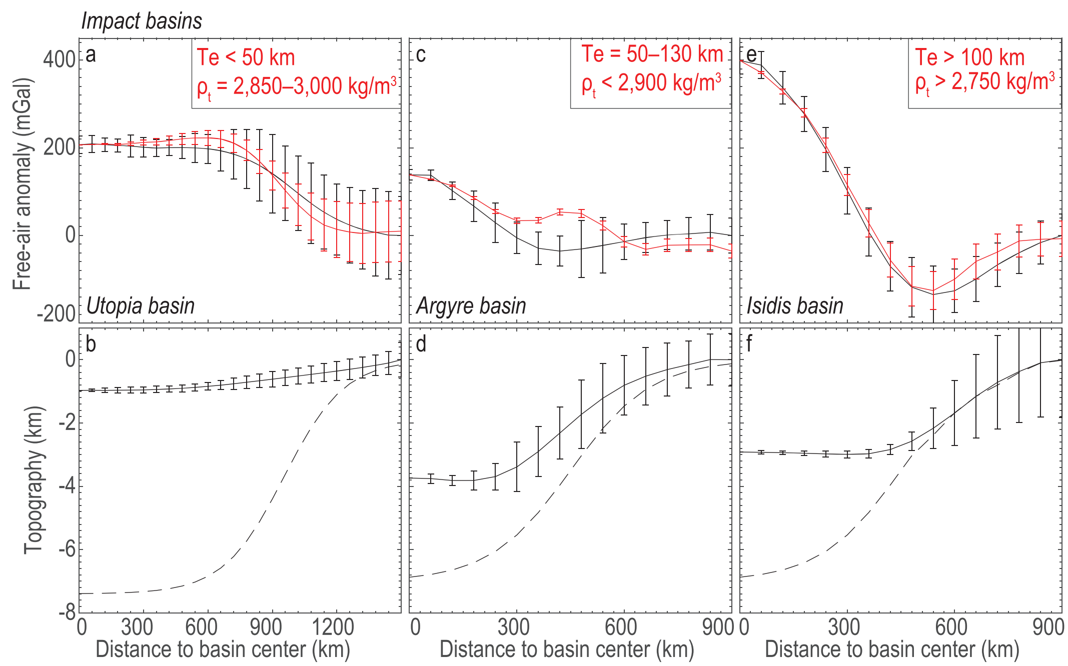

Figure 12. Comparisons between observed gravity profiles (gray) and accepted models (red) for the impact basins: (a) Utopia basin; (c) Argyre basin; and (e) Isidis basin. The curves with error bars in the top and bottom panels correspond to azimuthally averaged gravitational and topographic profiles. In the bottom panels (b, d, f), solid curves with error bars are observed topography, and dashed curves are assumed pre-infill topography.

For the northern polar cap, we estimate *Te* to be in the range of >190 km using the second model (Figure 9e), which is larger than the *Te* estimate of 60–120 km by Johnson et al. (2000) based on a flexural moat analysis of a circumpolar depression filled with Amazonian sediment deposits. However, the estimate of Johnson et al. (2000) is less reliable because it is uncertain whether the circumpolar deposits indeed correspond to a flexural moat induced by the polar ice loading. For the southern polar cap, our calculated *Te* range of >185 km (Figure 9g) is consistent with the *Te* estimation of >102 km by Wieczorek (2008). The difference is mainly because we assumed a fixed ρ_t of 1,000 kg/m^3, instead of a best fit range of 1,166–1,391 kg/m^3 by Wieczorek (2008). This interpretation can be confirmed by comparing our first model with varied ρ_t (Figures 9c–9d), yielding ρ_t of <1,400 kg/m^3.

All the above *Te* estimates for the two polar caps might be biased upward due to the ignorance of transient viscoelastic response of the Martian mantle to a complex loading and unloading history (Johnson et al., 2000). However, the relatively large magnitude of the polar *Te*, compared with other subregions, is supported by the estimation from observed substrata deflection based on radar sounding data. Using the radar sounding data, Plaut et al. (2007) and Phillips et al. (2008) estimated the *Te* to be >150 km for the southern pole and >300 km for the northern pole, respectively.

3.3. Volcanic Montes

We find large variations in *Te* for the volcanic montes (Figure 10 and Table 3). The surface density ρ_t is estimated to be >3,100 kg/m^3 with a best fit value of 3,300 kg/m^3 (i.e., the upper limit of the a priori range) for the investigated montes. The estimated parameter α tends to be −1, corresponding to buoyant subsurface loading due to a mantle plume and/or depleted mantle composition (Figure 2c), which has also been preferred by previous admittance analyses of Belleguic et al. (2005) and Beuthe et al. (2012). This interpretation is supported by the presence of recent volcanic activity (Neukum et al., 2004).

Of the three relatively large volcanoes (Figures 10a–10c), we estimate *Te* to be >105 km for Olympus Mons (Figure 10a); this value is larger but consistent with the estimates of >70 km by McGovern et al. (2004) and 53–133 km by Belleguic et al. (2005) considering surface loading only. In comparison, the systematic lower admittance for Alba and Elysium Montes (Figures 10b and 10c) indicates lower *Te*. For Alba Mons (Figure 10b), the spectral drop-off for degrees beyond 35 cannot be fitted by our uniform-parameter flexural models. A surface loading model with two different loading densities (Beuthe et al., 2012), however, successfully reproduced the spectral drop with a *Te* value of close to 0. The increase in *Te* from Elysium and Alba Montes to Olympus Mons likely indicates an increasing loading age of the main volcanic edifices, which is supported by surface geochemical compositions of the volcanoes (Baratoux et al., 2011).

For the three smaller Tharsis montes, smaller localization cap windows (Table 2) were used to isolate them from each other and from the long-wavelength Tharsis features (Figure 1a). The smaller localization windows left us with limited degree ranges for inversion (Figures 10d–10f) and thus likely less well-constrained parameters. Nevertheless, the observed admittance for Arsia Mons still provides a tight constraint on *Te* of <15 km (Figure 10d), which is consistent with an estimation of <35 km by Belleguic et al. (2005) and <10 km by Beuthe et al. (2012). In contrast, the *Te* estimate of >20 km by McGovern et al. (2004) is less reliable as it may be biased by their larger localization window with weaker spatial concentration. For Pavonis Mons (Figure 10e), we chose two degree ranges of <35 and >47, respectively, for separate inversions, because uniform-parameter flexural models cannot explain the descending admittance in the intermediate degree range of 36–46. For the lower degree range of 31–35, the parameter *Te* is not constrained; this may explain why McGovern et al. (2004) and Belleguic et al. (2005) found distinct *Te* estimates of <100 km and >50 km for the similar degree range. For the higher degree range of 47–64, we estimate *Te* to be <15 km. It is worth mentioning that Beuthe et al. (2012) provided a two-stage surface loading model to explain the full degree range of Pavonis Mons, yielding a first-stage *Te* of <40 km and a second-stage *Te* of 60–120 km. Our estimated *Te* for the higher degree range thus corresponds to their first-stage *Te* range. For Ascraeus Mons (Figure 10f), our estimated *Te* of >90 km for degrees lower than 41 is larger than but consistent with the *Te* estimate of >50 km for degrees 31–45 by Belleguic et al. (2005). Comparing the three Tharsis montes, the extremely low *Te* for Arsia Mons cannot be explained by its lower mantle potential temperature as inferred by the surface geochemical compositions (Baratoux et al., 2011), but are consistent with the presence of a decoupling layer in a thick crust (Grott & Breuer, 2010).

3.4. Valles Marineris

The prominent 4,000-km-long rift valley system, Valles Marineris, stretches for nearly a quarter of the planet's circumference. We have selected three segments, Ius, Melas, and Coprates Chasma to investigate the west-to-east variability in the lithospheric and loading states (Figure 1a and Table 2). From the diverse shapes of the localized admittance (Figure 11), we find the lowest *Te* range for Melas Chasma (middle segment), which is different from the previously suggested west-to-east decreasing trend by McGovern et al. (2002) and Beuthe et al. (2012). This implies a complex tectonic evolution history of Valles Marineris rather than being simply controlled by a magma source in the central Tharsis province. However, our estimated reductions in f and ρ_t from Ius to Coprates Chasma are consistent with the decrease in dike intensity with distance from the magma source (McGovern et al., 2002). It is worth noting that Beuthe et al. (2012) considered a more complex two-stage formation scenario (Andrews-Hanna, 2012; Davis & Andrews-Hanna, 2011) to yield lower *Te* for the earlier stage of sediment loading and larger *Te* for the later stage of sediment erosion.

3.5. Impact Basins

We estimate *Te* to be <50 km and ρ_t to be 2,850–3,000 kg/m^3 for the Utopia basin (Figure 12a) based on the axisymmetric profile of the free-air gravity anomaly. We estimate a larger *Te* range of 50–130 km for the Argyre basin (Figure 12c), with a ρ_t range of <2,900 kg/m^3. For the Isidis basin (Figure 12e), our estimated *Te* of >100 km is greater than those of the other two basins. Ritzer and Hauck (2009) estimated a consistent *Te* range of 100–180 km from the location of surrounding grabens. Our estimated ρ_t range of >2,750 kg/m^3 for the Isidis basin is also larger than those for the other two basins. The larger *Te* and ρ_t for the Isidis basin are required to explain the substantially larger free-air gravity anomaly of ~400 mGal. The relatively large ρ_t implies a larger component of volcanic infilling (during the Hesperian period, Ivanov et al., 2012) than the other two impact basins. In contrast, Utopia and Argyre basins likely act as a regional catchment mainly for sedimentary materials (Dohm et al., 2015), although the possibility of volcanic infilling cannot be excluded given the a priori ρ_t ranges of 2,900–3,300 kg/m^3 for basaltic infills (section 2.3).

Comparison with previous gravity studies of impact basins suggests that the inverted *Te* highly depends on the assumption of the pre-infill state. Relaxing the assumption of Airy isostasy and introducing an arbitrary compensation coefficient for the pre-infill basin, Ritzer and Hauck (2009) and Searls et al. (2006) found *Te* to

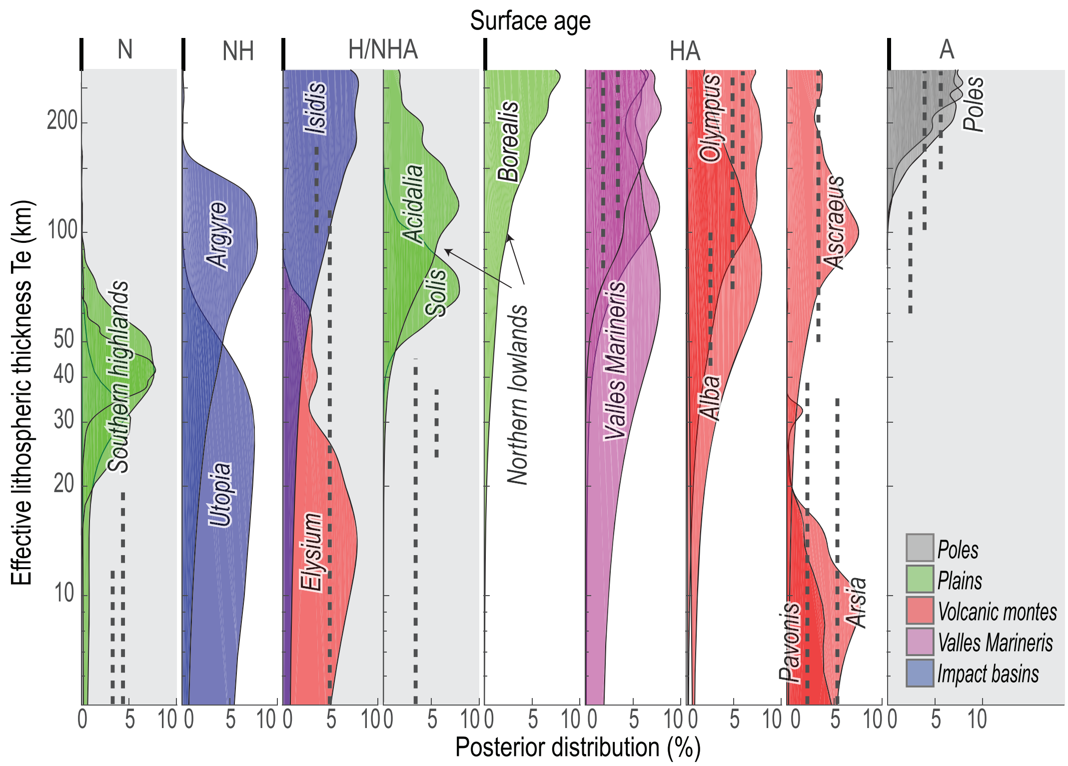

Figure 13. Estimated probability distribution of the regional *Te* (top left panels of Figures 6 and S8–S37) versus surface age periods (Table 2). N, H, and A correspond to the Noachian (4.1–3.8 Ga), Hesperian (3.8–3.0 Ga), and Amazonian (<3.0 Ga) periods, respectively. Green, red, blue, magenta, and gray colors correspond to regions of different tectonic types, that is, plains, volcanic, impact basins, rift valleys, and polar caps, respectively. Dashed vertical lines correspond to previous *Te* estimates listed in the last column of Table 3.

be unconstrained for the Isidis and Utopia basins. The results of Mancinelli et al. (2015) for the Isidis basin may be biased as they did not consider pre-infill basin depression. In addition, if we consider that some gravitational anomalies due to the viscoelastic relaxation of impact basins (Andrews-Hanna & Stewart, 2011; Freed et al., 2014; Melosh et al., 2013; Montesi, 2013) existed before the deposition of surface infilling, the absolute values of *Te* and ρ_t are likely to be lower than our current estimates. However, the comparative results remain valid: The surface deposits of the Isidis basin are associated with larger ρ_t and *Te* than those of the other two basins, assuming similar pre-infill compensation states.

4. Discussion

4.1. Comparison with Previous *Te* Estimates

The use of the latest gravity model with a higher spatial resolution does not improve the constraints on *Te*, because the theoretical models are less sensitive to *Te* in the degree range greater than ~60 (Figure 3a). In addition, the highest-degree spectra are commonly inconsistent with the uniform-parameter flexural models and thus are required to be excluded in the inversion (e.g., Figure 7). Nevertheless, the relative magnitude of our *Te* estimates, especially for subregions of the same tectonic type, is consistent with the recent gravity-based studies. The comparison between our solutions and previous estimates can be found in Table 3 and Figure 13.

For the plain regions (green patches in Figure 13), our *Te* estimates considering both surface and subsurface loading are notably larger than the estimates considering surface loading only (black dashed lines, from McGovern et al., 2004). This notable difference is due to different loading style assumptions. However, the hemispheric difference in *Te* between the northern lowlands and the southern highlands is robust, which is clearly shown in the free-air admittance and correlation observations (Figures 7 and 8). This hemispheric difference has also been found in a preliminary global *Te* model by Audet (2014).

Our solutions closely match the results of Belleguic et al. (2005) for the volcanic montes (red patches and corresponding black dashed lines in Figure 13), although we did not factor in the pressure term due to the deflection of the geoid as did Belleguic et al. (2005). Our *Te* estimates are expected to be more robust as the MCMC algorithm samples the parameter space more thoroughly. Beuthe et al. (2012) suggested two-stage surface loading models to fit the entire degree ranges for Alba and Pavonis Montes. However, *Te* then became highly unconstrained when combining together the two *Te* ranges for the two loading stages. For the impact basins (blue patches in Figure 13), our estimated *Te* ranges are narrower than the estimates by Searls et al. (2006) (unconstrained) and Ritzer and Hauck (2009) (black dashed line) with an additional free parameter (i.e., the compensation coefficient).

Comparison with *Te* estimates based on fault distribution or substrata deflection requires closer scrutiny due to the various interpretations of potential flexural features (e.g., Johnson et al., 2000; McGovern et al., 2002). Nevertheless, our gravity-based estimates are consistent with the *Te* estimates for Olympus Mons based on regional fault distribution (Comer et al., 1985) and for the polar caps based on substrata deflection in the radar sounding data (Phillips et al., 2008; Plaut et al., 2007).

4.2. Thermal Evolution and Spatial Variability

Our *Te* estimate for each subregion corresponds to the regional elastic thicknesses of the lithosphere averaged over the time period of tectonic loading. The variations in the *Te* estimates thus reflect both spatial heterogeneities and temporal changes. The increase in *Te* from the Noachian southern highlands to the Hesperian northern lowlands (green patches in Figure 13) is compatible with models of global cooling and heat flux reduction with time (e.g., McGovern et al., 2002; Zuber et al., 2000), although we cannot exclude the effects of spatial variability.

The spatial variability may be induced either by different thermal evolution paths such as after an early phase of plate tectonics (Spohn, 2001) or by different crustal thicknesses (Schumacher & Breuer, 2006). The increase in *Te* from the Noachian Elysium Mons to Olympus Mons (red patches in Figure 13) also follows the trend of plate cooling despite the age uncertainty for Olympus Mons (Noachian or Amazonian, Beuthe et al., 2012; Isherwood et al., 2013; Werner, 2009). Recent thermal evolution models (Grott & Breuer, 2008, 2009, 2010; Plesa et al., 2015, 2016) have considered the effects of variable crustal thickness and conductivity on thermal evolution. These models have successfully explained the gravity-based *Te* estimates (e.g., McGovern et al., 2004; Belleguic et al., 2005; Hoogenboom & Smrekar, 2006;Wieczorek, 2008), as well as extremely large *Te* of >300 km for the present northern pole based on radar sounding data (Phillips et al., 2008).

4.3. Density Estimates

While the high-resolution gravity models of the Moon have been shown to be powerful for determining the spatial variations in the crustal density (Besserer et al., 2014; Huang & Wieczorek, 2012; Wieczorek et al., 2013), the comparatively low resolution of the Martian gravity models unfortunately still preclude tight constraints on the regional variations in the crustal density. We estimate higher ρ_t in the Isidis basin than in the Utopia and Argyre basins, indicating greater volcanic infilling and less sedimentary deposition. For Valles Marineris, while our gravitational analyses permit either compacted sedimentary or basaltic crustal materials, geologic considerations favor a model of high-density basaltic composition (Andrews-Hanna, 2012; McGovern et al., 2002).

For the six volcanic montes that we investigated, we prefer a large ρ_t close to 3,300 kg/m^3, which is consistent with previous estimates based on gravity analysis (Belleguic et al., 2005; Beuthe et al., 2012; Goossens et al., 2017; McGovern et al., 2004). This ρ_t value corresponds to a pore-free grain density of ~3,550 kg/m^3, assuming a rock porosity of 10% (Britt & Consolmagno, 2003) and that the porosity space is filled with water. This ρ_t value is also close to the upper limit of the a priori range. The pore-free grain density for Martian meteorites (mainly basaltic shergottites) has been measured to be 3,100–3,700 kg/m^3 (Baratoux et al., 2014), yielding a bulk density of 2,890–3,430 kg/m^3. If a larger ρ_t is permitted due to either lower porosity or higher grain density, estimates of lower *Te* would be expected.

For the investigated plain regions, the crustal density (which is assumed to be equal to the loading density) is not well constrained. However, if the crustal density can be fixed at a given value (e.g., from global gravity/topography analysis), *Te* is likely to be better constrained. For example, if the crustal density is assumed to be 2,900 kg/m^3 (e.g., Wieczorek & Zuber, 2004) for Noachis Terra, *Te* would be estimated to be 25–50 km (calculated from the Markov chain in Figure 6), which is narrower than our current range of 30–60 km. If the crustal density is assumed to be 2,550 kg/m^3 instead (Goossens et al., 2017), *Te* would be estimated to be 45–70 km. For the hemispheric difference, Gamma-Ray-Spectrometer data suggest a grain density increase of ~100 kg/m^3 from the southern to northern plains (Baratoux et al., 2014). If this increase is applicable to the bulk crustal density, the topographic dichotomy should be largely supported by the Pratt compensation mechanism (Belleguic et al., 2005; Pauer & Breuer, 2008).

4.4. Limitations and Improvements of the Localized Inverse Spectral Method

Due to the nonuniqueness of gravitational inversion, *Te* cannot be constrained without assumptions on the loading condition (e.g., Forsyth, 1985; Lowry & Zhong, 2003; Neumann et al., 2004). In other words, the *Te* estimates depend substantially on the loading style assumptions and thus could be biased by unwarranted loading assumptions. The applicability of uncorrelated loading assumptions for continental lithosphere is still a subject of debate (Forsyth, 1985; McKenzie, 2003, 2016; Simons et al., 2000). For the polar caps, which may be partially supported by transient viscoelastic relaxation, our *Te* might be an overestimation (McKenzie, 2010). For the impact basins with nonflat pre-infill topography, spectral analysis is not applicable without the full knowledge of the spatial distribution of surface infilling or pre-infill state (section 3.4). Furthermore, the *Te* estimates might be biased because the admittance and correlation do not strictly follow Gaussian error distributions (Simons & Olhede, 2013). It is also not clear whether the admittance and correlation are statistically consistent when inverting for *Te*. Therefore, our use of acceptable ranges of *Te* is more meaningful than the single best fit values. Additionally, the use of relative values between regions is more meaningful than the absolute values.

To resolve the regional spatial variability in *Te*, it is required to localize the data in a region small enough so that uniform *Te* and loading style can be reasonably assumed. At the same time, the localization window needs to be large enough to retain the transition wavelengths from local compensation to lack of compensation (Figure 3a). Comparative tests using different localization techniques, for example, maximum entropy and wavelets (Kirby, 2014), and different window sizes are necessary to analyze the effect of the localization process in further studies. Due to the complex spectral observations for each individual subregion, only a portion of the degree range(s) can be used for fitting models of uniform parameters (see section 2.4; Beuthe et al., 2012). This may only be improved by taking into account multiple loading stages with additional parameters.

5. Conclusions

From the localized gravity/topography admittance and correlation spectra of 21 subregions on Mars within five distinct types of tectonic regimes, we inverted for the regional flexural and loading parameters for the subregions. Our analyses yield the following results:

1. Regional tectonics and loading styles greatly influence the localized flexural models and thus the *Te* estimates. For the plains, our estimated *Te* range assuming uncorrelated surface and subsurface loading is larger than the models assuming surface loading only. For the volcanic montes, our estimated *Te* range assuming correlated surface and subsurface loading is wider than the models assuming surface loading only.
2. The *Te* estimates of this study reflect the regional thermal states at the time of loading and are generally consistent with global cooling and lithospheric thickening models. Our *Te* estimates increase from the most ancient Noachian southern highlands (20–60 km) to the Hesperian northern lowlands (>90 km) and from the Hesperian Elysium Mons (<55 km) to the Hesperian/Amazonian Olympus Mons (>105 km).
3. The density estimates of this study are consistent with basaltic surface infilling for the volcanic montes and Isidis basin, in contrast to sedimentary infilling for the Utopia and Argyre basins.
4. We find a higher correlation between the surface and subsurface loading for the northern than the southern polar cap, which is likely due to a depression of the crust-mantle interface that has not yet rebounded from an old (Amazonian) ice cap of larger size than the present. We also find high correlation between the surface and subsurface loading for the northern plains, likely due to ancient (Noachian) features buried by long-term sediment and magmatic deposits.

Acknowledgments

The gravity model JGMRO120d and topography model MarsTopo719 used in this paper were retrieved from the Geosciences Node of NASA's Planetary Data System (http://pds-geosciences.wustl.edu/mro/mro-m-rss-5-sdp-v1/mrors_1xxx/data/shadr/) and from the SHTOOLS package (http://sourceforge.net/projects/shtools/), respectively. The MATLAB codes to reproduce the data analysis, parameter estimation, and key figures are available in a github repository (https://github.com/MinaDing/marslithosphere/tree/v1.0.0, DOI: 10.5281/zenodo.3530057). We are grateful to Mark Wieczorek and Frederik Simons for sharing relevant software online. We thank Ken Tanaka for providing a digital map of Mars chronographic ages. We thank Brandon Johnson for consultation on the loading processes of impact basins. We also thank Editor Laurent Montesi and Steven A. Hauck, as well as Patrick McGovern and anonymous reviewers for their invaluable feedbacks. This work was supported by National Natural Science Foundation of China (41806067, 41890813, 91628301 and U1606401), Key Laboratory of Ocean and Marginal Sea Geology, Chinese Academy of Sciences (OMG18-02), Chinese Academy of Sciences (Y4SL021001, QYZDY-SSW-DQC005 and 133244KYSB20180029), Southern Marine Science and Engineering Guangdong Laboratory (Guangzhou) (GML2019ZD0205), Radio Science Gravity investigation of the NASA Mars Reconnaissance Orbiter mission (M.T. Z.), and National Science Foundation (EAR 1220280) and Henry Bigelow Chair for Excellence in Oceanography (J.L.).

References

Anderson, S., & Grimm, R. E. (1998). Rift processes at the Valles Marineris, Mars: Constraints from gravity on necking and rate-dependent strength evolution. *Journal of Geophysical Research*, *103*(E5), 11,113–11,124. https://doi.org/10.1029/98JE00740

Andrews-Hanna, J. C. (2012). The formation of Valles Marineris: 3. Trough formation through super-isostasy, stress, sedimentation, and subsidence. *Journal of Geophysical Research*, *117*, E06002. https://doi.org/10.1029/2012JE004059

Andrews-Hanna, J. C., & Stewart, S. T. (2011). The crustal structure of Orientale and implications for basin formation. Presented at the 42nd Lunar and Planetary Science Conference, The Woodlands, TX, United States.

Andrews-Hanna, J. C., Zuber, M. T., & Banerdt, W. B. (2008). The Borealis basin and the origin of the martian crustal dichotomy. *Nature*, *453*(7199), 1212–1215. https://doi.org/10.1038/nature07011

Arkani-Hamed, J. (2000). Strength of Martian lithosphere beneath large volcanoes. *Journal of Geophysical Research*, *105*, 26,713–26,732. https://doi.org/10.1029/2000JE001267

Audet, P. (2014). Toward mapping the effective elastic thickness of planetary lithospheres from a spherical wavelet analysis of gravity and topography. *Physics of the Earth and Planetary Interiors*, *226*, 48–82. https://doi.org/10.1016/j.pepi.2013.09.011

Banerdt, W. B., Phillips, R. J., Sleep, N. H., & Saunders, R. S. (1982). Thick shell tectonics on one-plate planets: Applications to Mars. *Journal of Geophysical Research*, *87*(B12), 9723–9733. https://doi.org/198210.1029/JB087iB12p09723

Baratoux, D., Samuel, H., Michaut, C., Toplis, M. J., Monnereau, M., Wieczorek, M., et al. (2014). Petrological constraints on the density of the Martian crust. *Journal of Geophysical Research: Planets*, *119*, 1707–1727. https://doi.org/10.1002/2014JE004642

Baratoux, D., Toplis, M. J., Monnereau, M., & Gasnault, O. (2011). Thermal history of Mars inferred from orbital geochemistry of volcanic provinces. *Nature*, *472*(7343), 338–341. https://doi.org/10.1038/nature09903

Belleguic, V., Lognonné, P., & Wieczorek, M. (2005). Constraints on the Martian lithosphere from gravity and topography data. *Journal of Geophysical Research*, *110*, E11005. https://doi.org/10.1029/2005JE002437

Bendat, J. S., & Piersol, A. G. (2010). *Random data: Analysis and measurement procedures* (fourth ed.). New York: John Wiley & Sons, Inc.

Besserer, J., Nimmo, F., Wieczorek, M. A., Weber, R. C., Kiefer, W. S., McGovern, P. J., et al. (2014). GRAIL gravity constraints on the vertical and lateral density structure of the lunar crust. *Geophysical Research Letters*, *41*, 5771–5777. https://doi.org/10.1002/2014GL060240

Beuthe, M., Le Maistre, S., Rosenblatt, P., Pätzold, M., & Dehant, V. (2012). Density and lithospheric thickness of the Tharsis Province from MEX MaRS and MRO gravity data: Density and lithosphere of Tharsis. *Journal of Geophysical Research*, *117*, E04002. https://doi.org/10.1029/2011JE003976

Britt, D. T., & Consolmagno, G. (2003). Stony meteorite porosities and densities: A review of the data through 2001. *Meteoritics and Planetary Science*, *38*(8), 1161–1180.

Byrne, S. (2009). The polar deposits of Mars. *Annual Review of Earth and Planetary Sciences*, *37*(1), 535–560. https://doi.org/10.1146/annurev.earth.031208.100101

Byrne, S., & Murray, B. C. (2002). North polar stratigraphy and the paleo-erg of Mars. *Journal of Geophysical Research*, *107*(E6), 5044. https://doi.org/10.1029/2001JE001615

Carr, M. H., & Head, J. W. III (2010). Geologic history of Mars. *Earth and Planetary Science Letters*, *294*(3–4), 185–203. https://doi.org/10.1016/j.epsl.2009.06.042

Christensen, E. J., & Balmino, G. (1981). Development and analysis of a twelfth degree and order gravity model for Mars. *Journal of Geophysical Research*, *86*. https://doi.org/10.1029/JB086iB07p06382

Comer, R. P. (1983). Thick plate flexure. *Geophysical Journal International*, *72*(1), 101–113. https://doi.org/10.1111/j.1365-246X.1983.tb02807.x

Comer, R. P., Solomon, S. C., & Head, J. W. (1985). Mars: Thickness of the lithosphere from the tectonic response to volcanic loads. *Reviews of Geophysics*, *23*(1), 61–92. https://doi.org/10.1029/RG023i001p00061

Crosby, A. G. (2007). An assessment of the accuracy of admittance and coherence estimates using synthetic data. *Geophysical Journal International*, *171*(1), 25–54. https://doi.org/10.1111/j.1365-246X.2007.03520.x

Davis, B. J., & Andrews-Hanna, J. C. (2011). Flexural response to sediment erosion and unloading at Valles Marineris, Mars. Presented at the 42nd Lunar and Planetary Science Conference, The Woodlands, TX, United States.

Dohm, J. M., Hare, T. M., Robbins, S. J., Williams, J.-P., Soare, R. J., El-Maarry, M. R., et al. (2015). Geological and hydrological histories of the Argyre province, Mars. *Icarus*, *253*, 66–98. https://doi.org/10.1016/j.icarus.2015.02.017

Fishbaugh, K. E., & Head, J. W. (2001). Comparison of the north and south polar caps of Mars: New observations from MOLA data and discussion of some outstanding questions. *Icarus*, *154*(1), 145–161. https://doi.org/10.1006/icar.2001.6666

Fishbaugh, K. E., & Head, J. W. (2005). Origin and characteristics of the Mars north polar basal unit and implications for polar geologic history. *Icarus*, *174*(2), 444–474. https://doi.org/10.1016/j.icarus.2004.06.021

Forsyth, D. W. (1985). Subsurface loading and estimates of the flexural rigidity of continental lithosphere. *Journal of Geophysical Research*, *90*(B14), 12,623–12,632. https://doi.org/10.1029/JB090iB14p12623

Freed, A. M., Johnson, B. C., Blair, D. M., Melosh, H. J., Neumann, G. A., Phillips, R. J., et al. (2014). The formation of lunar mascon basins from impact to contemporary form. *Journal of Geophysical Research: Planets*, *119*, 2378–2397. https://doi.org/10.1002/2014JE004657

Frey, H. V., Shockey, K. M., Frey, E. L., Roark, J. H., & Sakimoto, S. E. H. (2001). A very large population of likely buried impact basins in the northern lowlands. Presented at the 32nd Annual Lunar and Planetary Science Conference, Houston, Texas.

Goossens, S., Sabaka, T. J., Genova, A., Mazarico, E., Nicholas, J. B., & Neumann, G. A. (2017). Evidence for a low bulk crustal density for Mars from gravity and topography. *Geophysical Research Letters*, *44*, 7686–7694. https://doi.org/10.1002/2017GL074172

Grott, M., & Breuer, D. (2008). The evolution of the Martian elastic lithosphere and implications for crustal and mantle rheology. *Icarus*, *193*(2), 503–515. https://doi.org/10.1016/j.icarus.2007.08.015

Grott, M., & Breuer, D. (2009). Implications of large elastic thicknesses for the composition and current thermal state of Mars. *Icarus*, *201*(2), 540–548. https://doi.org/10.1016/j.icarus.2009.01.020

Grott, M., & Breuer, D. (2010). On the spatial variability of the Martian elastic lithosphere thickness: Evidence for mantle plumes? *Journal of Geophysical Research*, *115*, E03005. https://doi.org/10.1029/2009JE003456

Grott, M., & Wieczorek, M. A. (2012). Density and lithospheric structure at Tyrrhena Patera, Mars, from gravity and topography data. *Icarus*, *221*(1), 43–52. https://doi.org/10.1016/j.icarus.2012.07.008

Gu, C., Marzouk, Y. M., & Toksöz, M. N. (2018). Waveform-based Bayesian full moment tensor inversion and uncertainty determination for the induced seismicity in an oil/gas field. *Geophysical Journal International*, *212*(3), 1963–1985. https://doi.org/10.1093/gji/ggx517

Haario, H., Saksman, E., & Tamminen, J. (2001). An adaptive Metropolis algorithm. *Bernoulli*, *7*(2), 223–242.

Hoogenboom, T., & Smrekar, S. (2006). Elastic thickness estimates for the northern lowlands of Mars. *Earth and Planetary Science Letters*, *248*(3–4), 830–839. https://doi.org/10.1016/j.epsl.2006.06.035

Howenstine, J. B., & Kiefer, W. S. (2005). Morphometry of large Martian impact craters. Presented at the 36th Annual Lunar and Planetary Science Conference, League City, Texas.

Huang, Q., & Wieczorek, M. A. (2012). Density and porosity of the lunar crust from gravity and topography. *Journal of Geophysical Research*, *117*, E05003. https://doi.org/10.1029/2012JE004062

Isherwood, R. J., Jozwiak, L. M., Jansen, J. C., & Andrews-Hanna, J. C. (2013). The volcanic history of Olympus Mons from paleo-topography and flexural modeling. *Earth and Planetary Science Letters*, *363*, 88–96. https://doi.org/10.1016/j.epsl.2012.12.020

Ivanov, M. A., Hiesinger, H., Erkeling, G., Hielscher, F. J., & Reiss, D. (2012). Major episodes of geologic history of Isidis Planitia on Mars. *Icarus*, *218*(1), 24–46. https://doi.org/10.1016/j.icarus.2011.11.029

Janle, P., & Erkul, E. (1991). Gravity studies of the Tharsis area on Mars. *Earth, Moon, and Planets*, *53*(3), 217–232. https://doi.org/10.1007/BF00055948

Johnson, C. L., Solomon, S. C., Head, J. W., Phillips, R. J., Smith, D. E., & Zuber, M. T. (2000). Lithospheric loading by the northern polar cap on Mars. *Icarus*, *144*(2), 313–328. https://doi.org/10.1006/icar.1999.6310

Kiefer, W. S., & Li, Q. (2009). Mantle convection controls the observed lateral variations in lithospheric thickness on present-day Mars. *Geophysical Research Letters*, *36*, L18203. https://doi.org/10.1029/2009GL039827

Kirby, J. F. (2014). Estimation of the effective elastic thickness of the lithosphere using inverse spectral methods: The state of the art. *Tectonophysics*, *631*, 87–116. https://doi.org/10.1016/j.tecto.2014.04.021

Konopliv, A. S., Park, R. S., & Folkner, W. M. (2016). An improved JPL Mars gravity field and orientation from Mars orbiter and lander tracking data. *Icarus*, *274*, 253–260. https://doi.org/10.1016/j.icarus.2016.02.052

Li, J., Andrews-Hanna, J. C., Sun, Y., Phillips, R. J., Plaut, J. J., & Zuber, M. T. (2012). Density variations within the south polar layered deposits of Mars. *Journal of Geophysical Research*, *117*, E04006. https://doi.org/10.1029/2011JE003937

Lowry, A. R., & Zhong, S. (2003). Surface versus internal loading of the Tharsis rise, Mars. *Journal of Geophysical Research*, *108*(E9), 5099. https://doi.org/10.1029/2003JE002111

Mancinelli, P., Mondini, A. C., Pauselli, C., & Federico, C. (2015). Impact and admittance modeling of the Isidis Planitia, Mars. *Planetary and Space Science*, *117*, 73–81. https://doi.org/10.1016/j.pss.2015.04.019

Marinova, M. M., Aharonson, O., & Asphaug, E. (2008). Mega-impact formation of the Mars hemispheric dichotomy. *Nature*, *453*(7199), 1216–1219. https://doi.org/10.1038/nature07070

McGovern, P. J., Solomon, S. C., Smith, D. E., Zuber, M. T., Simons, M., Wieczorek, M. A., et al. (2002). Localized gravity/topography admittance and correlation spectra on Mars: Implications for regional and global evolution. *Journal of Geophysical Research*, *107*(E12), 5136. https://doi.org/10.1029/2002JE001854

McGovern, P. J., Solomon, S. C., Smith, D. E., Zuber, M. T., Simons, M., Wieczorek, M. A., et al. (2004). Correction to "Localized gravity/topography admittance and correlation spectra on Mars: Implications for regional and global evolution". *Journal of Geophysical Research*, *109*, E07007. https://doi.org/10.1029/2004JE002286

McKenzie, D. (2003). Estimating *Te* in the presence of internal loads. *Journal of Geophysical Research*, *108*(B9), 2438. https://doi.org/10.1029/2002JB001766

McKenzie, D. (2010). The influence of dynamically supported topography on estimates of *Te*. *Earth and Planetary Science Letters*, *295*(1–2), 127–138. https://doi.org/10.1016/j.epsl.2010.03.033

McKenzie, D. (2016). A note on estimating *Te* from Bouguer coherence. *International Journal on Geomathematics*, *7*(1), 103–116. https://doi.org/10.1007/s13137-015-0078-4

McKenzie, D., Barnett, D. N., & Yuan, D.-N. (2002). The relationship between Martian gravity and topography. *Earth and Planetary Science Letters*, *195*(1–2), 1–16. https://doi.org/10.1016/S0012-821X(01)00555-6

Melosh, H. J., Freed, A. M., Johnson, B. C., Blair, D. M., Andrews-Hanna, J. C., Neumann, G. A., et al. (2013). The origin of lunar mascon basins. *Science*, *340*(6140), 1552–1555. https://doi.org/10.1126/science.1235768

Miller, J. W., & Dunson, D. B. (2019). Robust Bayesian inference via coarsening. *Journal of the American Statistical Association*, *114*(527), 1113–1125. https://doi.org/10.1080/01621459.2018.1469995

Montesi, L. G. J. (2013). Solving the mascon mystery. *Science*, *340*(6140), 1535–1536. https://doi.org/10.1126/science.1238099

Neukum, G., Jaumann, R., Hoffmann, H., Hauber, E., Head, J. W., Basilevsky, A. T., et al. (2004). Recent and episodic volcanic and glacial activity on Mars revealed by the High Resolution Stereo Camera. *Nature*, *432*(7020), 971–979. https://doi.org/10.1038/nature03231

Neumann, G. A., Zuber, M. T., Wieczorek, M. A., McGovern, P. J., Lemoine, F. G., & Smith, D. E. (2004). Crustal structure of Mars from gravity and topography. *Journal of Geophysical Research*, *109*, E08002. https://doi.org/10.1029/2004JE002262

Pauer, M., & Breuer, D. (2008). Constraints on the maximum crustal density from gravity–topography modeling: Applications to the southern highlands of Mars. *Earth and Planetary Science Letters*, *276*(3–4), 253–261. https://doi.org/10.1016/j.epsl.2008.09.014

Phillips, R. J., Zuber, M. T., Smrekar, S. E., Mellon, M. T., Head, J. W., Tanaka, K. L., et al. (2008). Mars north polar deposits: Stratigraphy, age, and geodynamical response. *Science*, *320*(5880), 1182–1185. https://doi.org/10.1126/science.1157546

Phillips, R. J., Zuber, M. T., Solomon, S. C., Golombek, M. P., Jakosky, B. M., Banerdt, W. B., et al. (2001). Ancient geodynamics and global-scale hydrology on Mars. *Science*, *291*(5513), 2587–2591. https://doi.org/10.1126/science.1058701

Picardi, G., Plaut, J. J., Biccari, D., Bombaci, O., Calabrese, D., Cartacci, M., et al. (2005). Radar soundings of the subsurface of Mars. *Science*, *310*(5756), 1925–1928. https://doi.org/10.1126/science.1122165

Plaut, J. J., Picardi, G., Safaeinili, A., Ivanov, A. B., Milkovich, S. M., Cicchetti, A., et al. (2007). Subsurface radar sounding of the south polar layered deposits of Mars. *Science*, *316*(5821), 92–95. https://doi.org/10.1126/science.1139672

Plesa, A.-C., Grott, M., Tosi, N., Breuer, D., Spohn, T., & Wieczorek, M. A. (2016). How large are present-day heat flux variations across the surface of Mars? *Journal of Geophysical Research: Planets*, *121*, 2386–2403. https://doi.org/10.1002/2016JE005126

Plesa, A.-C., Tosi, N., Grott, M., & Breuer, D. (2015). Thermal evolution and Urey ratio of Mars. *Journal of Geophysical Research: Planets*, *120*, 995–1010. https://doi.org/10.1002/2014JE004748

Ritzer, J. A., & Hauck, S. A. (2009). Lithospheric structure and tectonics at Isidis Planitia, Mars. *Icarus*, *201*(2), 528–539. https://doi.org/10.1016/j.icarus.2009.01.025

Schultz, R. A., & Lin, J. (2001). Three-dimensional normal faulting models of the Valles Marineris, Mars, and geodynamic implications. *Journal of Geophysical Research*, *106*(B8), 16,549–16,566. https://doi.org/10.1029/2001JB000378

Schumacher, S., & Breuer, D. (2006). Influence of a variable thermal conductivity on the thermochemical evolution of Mars. *Journal of Geophysical Research*, *111*, E02006. https://doi.org/10.1029/2005JE002429

Searls, M. L., Banerdt, W. B., & Phillips, R. J. (2006). Utopia and Hellas basins, Mars: Twins separated at birth. *Journal of Geophysical Research*, *111*, E08005. https://doi.org/10.1029/2005JE002666
Simons, F. J., & Olhede, S. C. (2013). Maximum-likelihood estimation of lithospheric flexural rigidity, initial-loading fraction and load correlation, under isotropy. *Geophysical Journal International*, 1300–1342. https://doi.org/10.1093/gji/ggt056
Simons, F. J., Zuber, M. T., & Korenaga, J. (2000). Isostatic response of the Australian lithosphere: Estimation of effective elastic thickness and anisotropy using multitaper spectral analysis. *Journal of Geophysical Research*, *105*, 19. https://doi.org/10.1029/2000JB900157
Sleep, N. H., & Phillips, R. J. (1985). Gravity and lithospheric stress on the terrestrial planets with reference to the Tharsis region of Mars. *Journal of Geophysical Research*, *90*, 4469–4489. https://doi.org/10.1029/JB090iB06p04469
Smith, A. M., Zuber, M. T., Frey, H. V., Gravin, J. B., Head, J. W., Muhlean, D. O., et al. (2001). Mars Orbiter Laser Altimeter: Experiment summary after the first year of global mapping of Mars. *Journal of Geophysical Research*, *106*(E10), 23689–23722. https://doi.org/10.1029/2000JE001364
Smith, R. C. (2013). *Uncertainty quantification: Theory, implementation, and applications*. Beaverton, United States: SIAM.
Solomon, S. C., & Head, J. W. (1990). Heterogeneities in the thickness of the elastic lithosphere of Mars: Constraints on heat flow and internal dynamics. *Journal of Geophysical Research*, *95*, 11,073–11,083. https://doi.org/10.1029/JB095iB07p11073
Spohn, T. (2001). The longevity of lunar volcanism: Implications of thermal evolution calculations with 2D and 3D mantle convection models. *Icarus*, *149*(1), 54–65. https://doi.org/10.1006/icar.2000.6514
Tanaka, K. L., Robbins, S. J., Fortezzo, C. M., Skinner, J. A., & Hare, T. M. (2013). The digital global geologic map of Mars: Chronostratigraphic ages, topographic and crater morphologic characteristics, and updated resurfacing history. *Planetary and Space Science*. https://doi.org/10.1016/j.pss.2013.03.006
Thomson, B. J., & Head, J. W. (2001). Utopia Basin, Mars: Characterization of topography and morphology and assessment of the origin and evolution of basin internal structure. *Journal of Geophysical Research*, *106*(E10), 23,209–23,230. https://doi.org/10.1029/2000JE001355
Turcotte, D. L., Willemann, R. J., Haxby, W. F., & Norberry, J. (1981). Role of membrane stresses in the support of planetary topography. *Journal of Geophysical Research*, *86*(B5), 3951–3959. https://doi.org/10.1029/JB086iB05p03951
Watters, T. R., Leuschen, C. J., Plaut, J. J., Picardi, G., Safaeinili, A., Clifford, S. M., et al. (2006). MARSIS radar sounder evidence of buried basins in the northern lowlands of Mars. *Nature*, *444*(7121), 905–908. https://doi.org/10.1038/nature05356
Watts, A. B. (2001). *Isostasy and flexure of the lithosphere*. Cambridge: Cambridge University Press.
Werner, S. C. (2008). The early Martian evolution—Constraints from basin formation ages. *Icarus*, *195*(1), 45–60. https://doi.org/10.1016/j.icarus.2007.12.008
Werner, S. C. (2009). The global Martian volcanic evolutionary history. *Icarus*, *201*(1), 44–68.
Wieczorek, M. A. (2007). The gravity and topography of the terrestrial planets. *Treatise on Geophysics*, *10*, 165–206.
Wieczorek, M. A. (2008). Constraints on the composition of the Martian south polar cap from gravity and topography. *Icarus*, *196*(2), 506–517. https://doi.org/10.1016/j.icarus.2007.10.026
Wieczorek, M. A., Neumann, G. A., Nimmo, F., Kiefer, W. S., Taylor, G. J., Melosh, H. J., et al. (2013). The crust of the Moon as seen by GRAIL. *Science*, *339*(6120), 671–675. https://doi.org/10.1126/science.1231530
Wieczorek, M. A., & Simons, F. J. (2005). Localized spectral analysis on the sphere. *Geophysical Journal International*, *162*(3), 655–675. https://doi.org/10.1111/j.1365-246X.2005.02687.x
Wieczorek, M. A., & Simons, F. J. (2007). Minimum-variance multitaper spectral estimation on the sphere. *Journal of Fourier Analysis and Applications*, *13*(6), 665–692. https://doi.org/10.1007/s00041-006-6904-1
Wieczorek, M. A., & Zuber, M. T. (2004). Thickness of the Martian crust: Improved constraints from geoid-to-topography ratios. *Journal of Geophysical Research*, *109*, E01009. https://doi.org/10.1029/2003JE002153
Wilhelms, D. E., & Squyres, S. W. (1984). The Martian hemispheric dichotomy may be due to a giant impact. *Nature*, *309*(5964), 138. https://doi.org/10.1038/309138a0
Wolf, D. (1985). Thick-plate flexure re-examined. *Geophysical Journal International*, *80*(1), 265–273. https://doi.org/10.1111/j.1365-246X.1985.tb05090.x
Zhong, S. (2002). Effects of lithosphere on the long-wavelength gravity anomalies and their implications for the formation of the Tharsis rise on Mars. *Journal of Geophysical Research*, *107*(E7), 5054. https://doi.org/10.1029/2001JE001589
Zhong, S., & Zuber, M. T. (2001). Degree-1 mantle convection and the crustal dichotomy on Mars. *Earth and Planetary Science Letters*, *189*(1), 75–84.
Zhou, S. (1991). A model of thick plate deformation and its application to the isostatic movements due to surface, subsurface and internal loadings. *Geophysical Journal International*, *105*(2), 381–395. https://doi.org/10.1111/j.1365-246X.1991.tb06720.x
Zuber, M. T. (2001). The crust and mantle of Mars. *Nature*, *412*(6843), 220–227. https://doi.org/10.1038/35084163
Zuber, M. T., Smith, D. E., Solomon, S. C., Muhlean, D. O., Head, J. W., Garvin, J. B., et al. (1992). The Mars Observer laser altimeter investigation. *Journal of Geophysical Research*, *97*(E5), 7781–7797. https://doi.org/10.1029/92JE00341
Zuber, M. T., Solomon, S. C., Phillips, R. J., Smith, D. E., Tyler, G. L., Aharonson, O., et al. (2000). Internal structure and early thermal evolution of Mars from Mars Global Surveyor topography and gravity. *Science*, *287*(5459), 1788–1793. https://doi.org/10.1126/science.287.5459.1788

References From the Supporting Information

Hastings, W. K. (1970). Monte Carlo sampling methods using Markov chains and their applications. *Biometrika*, *57*(1), 97–109. https://doi.org/10.1093/biomet/57.1.97
Metropolis, N., Rosenbluth, A. W., Rosenbluth, M. N., Teller, A. H., & Teller, E. (1953). Equation of state calculations by fast computing machines. *Journal of Chemical Physics*, *21*(6), 1087–1092. https://doi.org/10.1063/1.1699114